

## Additively manufactured functionally graded biodegradable porous iron

Li, Yageng; Jahr, H.; Pavanram, P.; Bobbert, Françoise; Paggi, U.; Zhang, X. Y.; Pouran, B.; Leeftang, M. A.; Weinans, H.; Zhou, Jie

**DOI**

[10.1016/j.actbio.2019.07.013](https://doi.org/10.1016/j.actbio.2019.07.013)

**Publication date**

2019

**Document Version**

Final published version

**Published in**

Acta Biomaterialia

**Citation (APA)**

Li, Y., Jahr, H., Pavanram, P., Bobbert, F., Paggi, U., Zhang, X. Y., Pouran, B., Leeftang, M. A., Weinans, H., Zhou, J., & Zadpoor, A. A. (2019). Additively manufactured functionally graded biodegradable porous iron. *Acta Biomaterialia*, 96, 646-661. <https://doi.org/10.1016/j.actbio.2019.07.013>

**Important note**

To cite this publication, please use the final published version (if applicable).  
Please check the document version above.

**Copyright**

Other than for strictly personal use, it is not permitted to download, forward or distribute the text or part of it, without the consent of the author(s) and/or copyright holder(s), unless the work is under an open content license such as Creative Commons.

**Takedown policy**

Please contact us and provide details if you believe this document breaches copyrights.  
We will remove access to the work immediately and investigate your claim.



Full length article

## Additively manufactured functionally graded biodegradable porous iron

Y. Li <sup>a,\*</sup>, H. Jahr <sup>b,c</sup>, P. Pavanram <sup>b</sup>, F.S.L. Bobbert <sup>a</sup>, U. Puggi <sup>d,e</sup>, X.-Y. Zhang <sup>f</sup>, B. Pouran <sup>a,g</sup>, M.A. Leeflang <sup>a</sup>, H. Weinans <sup>a,g</sup>, J. Zhou <sup>a,1</sup>, A.A. Zadpoor <sup>a,1</sup><sup>a</sup> Department of Biomechanical Engineering, Delft University of Technology, Delft 2628 CD, The Netherlands<sup>b</sup> Department of Anatomy and Cell Biology, University Hospital RWTH Aachen, Aachen 52074, Germany<sup>c</sup> Department of Orthopedic Surgery, Maastricht UMC+, Maastricht 6202 AZ, The Netherlands<sup>d</sup> 3D Systems – LayerWise NV, Grauwmeer 14, Leuven 3001, Belgium<sup>e</sup> KU Leuven Department of Mechanical Engineering, Kasteelpark Arenberg 44, Leuven 3001, Belgium<sup>f</sup> Department of Mechanical Engineering, Tsinghua University, Beijing 10004, China<sup>g</sup> Department of Orthopedics, UMC Utrecht, Heidelberglaan 100, Utrecht 3584CX, The Netherlands

## ARTICLE INFO

## Article history:

Received 30 April 2019

Received in revised form 3 July 2019

Accepted 9 July 2019

Available online 11 July 2019

## Keywords:

Additive manufacturing

Functionally graded material

Permeability

Biodegradation

Mechanical properties

Biocompatibility

## ABSTRACT

Additively manufactured (AM) functionally graded porous metallic biomaterials offer unique opportunities to satisfy the contradictory design requirements of an ideal bone substitute. However, no functionally graded porous structures have ever been 3D-printed from biodegradable metals, even though biodegradability is crucial both for full tissue regeneration and for the prevention of implant-associated infections in the long term. Here, we present the first ever report on AM functionally graded biodegradable porous metallic biomaterials. We made use of a diamond unit cell for the topological design of four different types of porous structures including two functionally graded structures and two reference uniform structures. Specimens were then fabricated from pure iron powder using selective laser melting (SLM), followed by experimental and computational analyses of their permeability, dynamic biodegradation behavior, mechanical properties, and cytocompatibility. It was found that the topological design with functional gradients controlled the fluid flow, mass transport properties and biodegradation behavior of the AM porous iron specimens, as up to 4-fold variations in permeability and up to 3-fold variations in biodegradation rate were observed for the different experimental groups. After 4 weeks of *in vitro* biodegradation, the AM porous scaffolds lost 5–16% of their weight. This falls into the desired range of biodegradation rates for bone substitution and confirms our hypothesis that topological design could indeed accelerate the biodegradation of otherwise slowly degrading metals, like iron. Even after 4 weeks of biodegradation, the mechanical properties of the specimens (*i.e.*,  $E = 0.5\text{--}2.1$  GPa,  $\sigma_y = 8\text{--}48$  MPa) remained within the range of the values reported for trabecular bone. Design-dependent cell viability did not differ from gold standard controls for up to 48 h. This study clearly shows the great potential of AM functionally graded porous iron as a bone substituting material. Moreover, we demonstrate that complex topological design permits the control of mechanical properties, degradation behavior of AM porous metallic biomaterials.

## Statement of Significance

No functionally graded porous structures have ever been 3D-printed from biodegradable metals, even though biodegradability is crucial both for full tissue regeneration and for the prevention of implant-associated infections in the long term. Here, we present the first report on 3D-printed functionally graded biodegradable porous metallic biomaterials. Our results suggest that topological design in general, and functional gradients in particular can be used as an important tool for adjusting the biodegradation behavior of AM porous metallic biomaterials. The biodegradation rate and mass transport properties of AM porous iron can be increased while maintaining the bone-mimicking mechanical properties of these biomaterials. The observations reported here underline the importance of proper topological design in the development of AM porous biodegradable metals.

© 2019 Acta Materialia Inc. Published by Elsevier Ltd. All rights reserved.

\* Corresponding author.

E-mail address: [y.li-7@tudelft.nl](mailto:y.li-7@tudelft.nl) (Y. Li).<sup>1</sup> Authors contributed equally to the study.

## 1. Introduction

The emergence of additive manufacturing (AM) techniques has provided unprecedented opportunities for the fabrication of porous metallic bone substitutes with promising bone regeneration capabilities [1–3]. The topological design of AM porous biomaterials can be precisely controlled and customized [4] with the aim of mimicking the mechanical properties of bone [5], facilitating cell proliferation and differentiation, and ultimately enhancing bone tissue regeneration [6]. During the last few years, a large number of AM porous metallic biomaterials have been investigated including those made from titanium alloys [7–9], stainless steel [10], cobalt-chromium alloys [11], and tantalum [12]. Most of these porous biomaterials possess complex, yet highly ordered micro-architectures that are made of regular unit cells designed through polyhedral arrangements of multiple struts (*i.e.*, beam-like structural elements). This leads to a homogeneous distribution of material properties throughout the entire porous structure [13]. A homogenous distribution of material properties is, however, not consistent with what is found in human bone where highly graded and non-uniform micro-architectures are present [14]. All types of human bones (*i.e.*, long, short, flat or irregular) show a gradual change in porosity from a compact outer cortical shell towards the spongy inner cancellous tissue. Other examples are the relative porosity and direction of trabecular structures in long bones (*e.g.*, femoral head and neck region or distal radius), which are both highly graded and dependent on the local values of mechanical stimuli (*e.g.*, strain energy density) [15–19]. It is therefore imperative that AM porous biomaterials mimic the natural gradual structures of human bones, particularly given the fact that they will be eventually surrounded by pockets of bony tissue with gradual micro-architecture [20] and biomechanical performance [21]. Furthermore, meeting the incompatible and sometimes contradictory design requirements of bone substitutes is often impossible without allowing for graded designs. For example, recent studies have clearly indicated that bone substitutes need to possess a high level of porosity (and, thus, permeability) to facilitate nutrient perfusion and cell viability [22]. However, highly porous scaffolds usually exhibit inadequate mechanical strength and low cell seeding efficiency [23]. Reconciling these contradictory design requirements limits the application of uniform topologies and calls for graded designs [24].

In addition to the above-mentioned advantages, functionally graded porous structures exhibit higher strength, ductility, and energy absorption capacity as compared to those of uniform porous structures [21,24–26]. The deformation behavior of functionally graded porous structures has been found to be smooth and continuous (during compression) without the formation of diagonal shear bands [21,27]. Finally, AM graded porous scaffolds have been found to result in high cell seeding efficiency [22,23,28] and to accelerate bone defect regeneration [29,30].

Although graded designs of AM porous biomaterials made from non-biodegradable metals such as titanium or cobalt-chrome alloys can improve the short-term performance of bone substitutes, they may hinder full regeneration of bony defects, given that part of the mechanical load will be permanently carried by the implant. Moreover, foreign objects, such as metallic implants, may elicit constant physical irritation and chronic local inflammation [31], which may necessitate revision surgery. Finally, non-biodegradable implants inflict the perpetual risk of incurring usually recurrent and difficult-to-treat implant-associated infections upon patients [32].

AM porous biomaterials made from biodegradable metals could solve the above-mentioned problems. However, only a few reports of direct printing of topologically ordered porous biodegradable metals are available. The first papers on this topic have appeared

very recently [33–38], with direct metal printing (*i.e.*, selective laser melting) being used for the fabrication of AM porous magnesium alloys, iron, iron-based alloys and zinc. AM of functionally graded, biodegradable metals has, however, not yet been reported.

Here, for the first time, we report the direct printing of a functionally graded biodegradable porous metal (*i.e.*, pure iron) using selective laser melting (SLM). Among biodegradable metals, inexpensive pure iron is a promising material and as it does not release hydrogen during biodegradation [39]. While a number of animal studies have shown good biocompatibility of iron-based biomaterials [40,41], their low *in vivo* degradation rate [41] is a clear disadvantage. However, AM porous metallic biomaterials generally have much larger surface areas as compared to their solid counterparts [42], which would be an important advantage for the materials that otherwise degrade too slowly, such as iron and its alloys. Moreover, as the biodegradation behavior of AM porous iron is topology-dependent, the presence of a functional gradient opens up new opportunities for adjusting the biodegradation behavior of porous iron. We, therefore, designed and additively manufactured four groups of AM porous iron specimens, namely two types of functionally graded porous specimens and two uniform (*i.e.*, reference) porous specimens. We then performed a comprehensive study on the mechanical behavior, permeability, biodegradation behavior, and cytocompatibility of these four groups using computational and experimental approaches.

## 2. Material and methods

### 2.1. Scaffold manufacturing and post processing

Four different types of specimens (Fig. 1a, b) based on a 1.4 mm diamond unit cell were designed using the software Element (nTopology, USA). The experimental groups included a uniform structure with a 0.2 mm strut thickness (S0.2), a functionally graded porous structure with a strut thickness changing from 0.2 mm on the periphery to 0.4 mm in the center (Dense-in), a functionally graded porous structure with strut thickness starting from 0.4 mm on the periphery and decreasing to 0.2 mm in the center (Dense-out), and a uniform porous structure with a strut thickness of 0.4 mm (S0.4) (Fig. 1a). Specimens were produced with a ProX DMP 320 machine (3D Systems, Belgium). The iron powder employed was gas atomized in nitrogen (Material Technology Innovations Co., Ltd., China) and had the following characteristics: purity: 99.88%; particle sizes: D10 = 32  $\mu\text{m}$ , D50 = 48  $\mu\text{m}$ , and D90 = 71  $\mu\text{m}$ ; morphology: spherical; apparent density: 4.09 g/cm<sup>3</sup>; tap density: 4.88 g/cm<sup>3</sup>; angle of repose: 157°; carbon content: 0.0044%. The specimens were built employing a layer thickness of 30  $\mu\text{m}$  on a steel baseplate. Contour and hatch vectors were used as the scanning strategy (energy densities: 0.33 W/mm and 0.65 W/mm, respectively) for most of the specimen, except for the specimens with 0.2 mm thick struts, in which case only contour was needed. Specimen removal was performed by means of electrical discharge machining (EDM). Powder particles entrapped in pores were removed through ultrasonic cleaning in 96% ethanol for 20 min. Then, the specimen were chemically cleaned in 50% HCl for 1 min to remove residuals from EDM and loose powder particles, followed by 5 min ultrasonic cleaning in 96% ethanol to wash the residual HCl out.

### 2.2. Morphological characterization

The iron scaffolds were imaged using micro-computed tomography (micro-CT) (Quantum FX, Perkin Elmer, USA) at a tube current of 180  $\mu\text{A}$ , a tube voltage of 90 kV, a scan time of 3 min, and a resolution of (30  $\mu\text{m}$ )<sup>3</sup> with a total of 3600 projections. Micro-

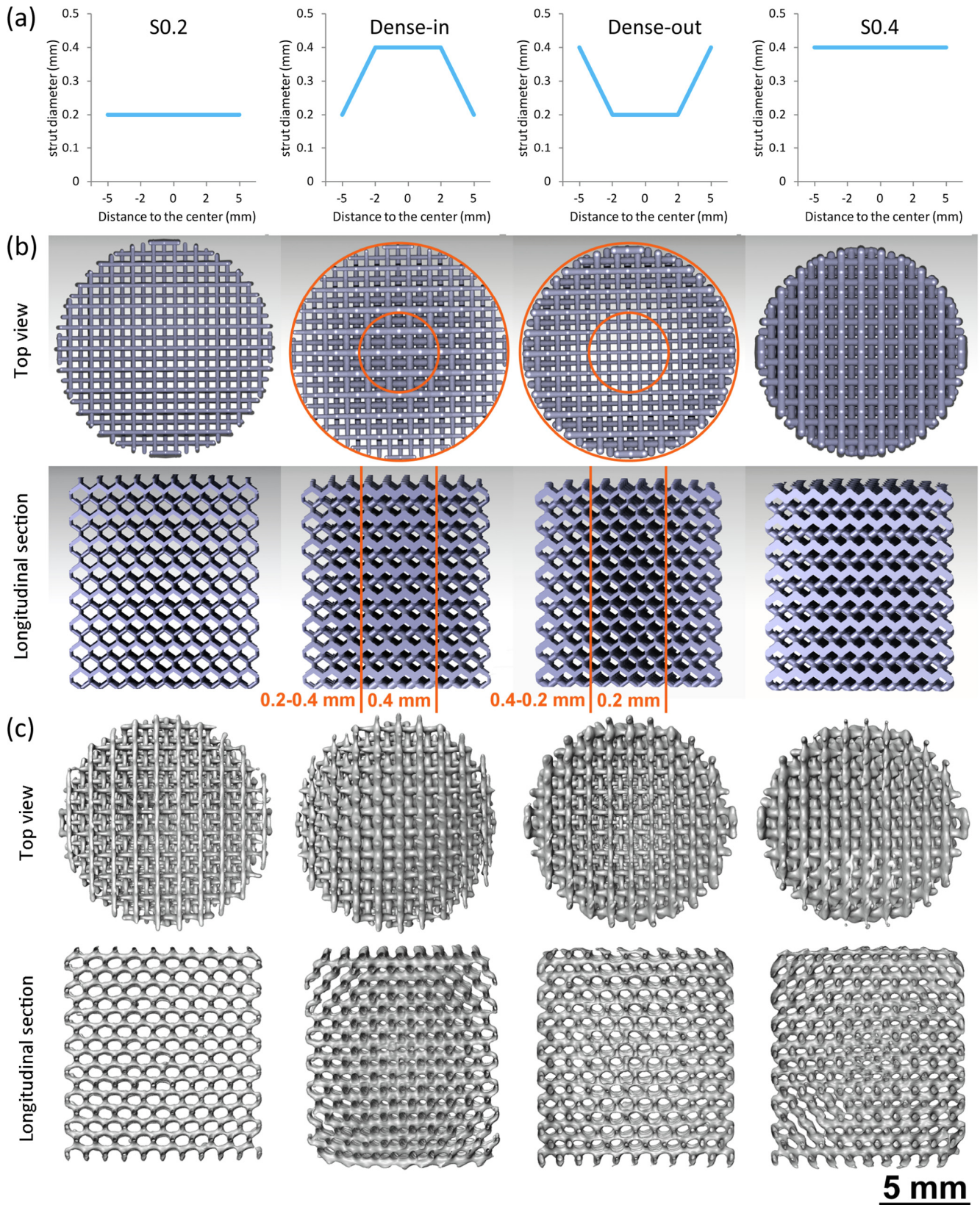


**Fig. 1.** The four different topological designs of the specimens from the S0.2, Dense-in, Dense-out, and S0.4 groups: (a) strut size distribution, (b) top view and longitudinal cross-section of the CAD models, and (c) the micro-CT reconstructions of the AM porous iron specimens.

CT images were automatically reconstructed and converted into a series of 2D images using Analyze 11.0 (Perkin Elmer, USA). The images were subsequently exported to FIJI (NIH, Bethesda, MD,

USA) and locally thresholded using the Bernsen algorithm (radius = 20). This allowed for accurate segmentation of the scaffolds and capturing their morphological features. Afterwards, a

number of circular regions of interest (ROIs) with a diameter of 10 mm were created on the cross-section of the scaffolds. The porosity (defined as the ratio of the void volume to the scaffold volume), average strut thickness (Tb.Th), and average strut spacing (Tb.Sp) (i.e., pore size), were then calculated using BoneJ (a plugin of Fiji).

In addition, a weighing method was used to determine the porosity of the specimens of the four groups based on the following equation:  $Porosity = 1 - (W_{iron}/V_{bulk})/\rho_{iron}$ , where  $W_{iron}$  is the weight of the specimen,  $V_{bulk}$  the bulk volume of the scaffold, and  $\rho_{iron}$  the theoretical density of pure iron.

### 2.3. Microstructural characterization

The microstructures of both thin and thick struts of the as-built specimens were examined using a digital optical microscope (Keyence VHX5000) after etching by a 5% Nital reagent (5 ml HNO<sub>3</sub> per 100 ml C<sub>2</sub>H<sub>5</sub>OH). The average grain size was measured using the line intercept method (based on three randomly chosen lines).

### 2.4. Permeability measurements

The falling head method was used, where a standpipe provided the water head and a pressure gauge measured the water pressure at the bottom of the standpipe. We used a vacuum pump to fill the standpipe with water, a chamber to host the scaffold, and a reservoir for water collection (Fig. 2a). The water pressure was measured just above the porous biomaterial and registered every two seconds in LabView (v.11.0). The measured pressure corresponded to the momentary height of the water column. Three specimens from each of the four experimental groups were used for permeability measurements. The permeability,  $k$ , was calculated using the following equation [43]:

$$k = \frac{a}{A} \frac{L}{t} \ln \frac{H_1}{H_2} \frac{\mu}{\rho g} = \frac{B}{A} / t$$

where  $a$  and  $A$  are, respectively, the cross-sectional areas of the standpipe and the specimen,  $L$  is the height of the specimen,  $H_1$  and  $H_2$  are the water levels at time points  $t_0$  and  $t_i$ , respectively,  $t$

equals to  $t_i - t_0$ , and  $\mu$  and  $\rho$  are the dynamic viscosity and density of water, respectively.  $B/A$  was plotted against time and extrapolated using a power function until the velocity of water approached zero. Then, the slope of this graph was used to calculate the permeability coefficient. As Darcy's law is only applicable when the Reynolds number is below 10, the slope was only taken in the region where the Reynolds number was between 1 and 10.

Computer simulations were performed on AM porous iron models using the computational fluid dynamics (CFD) solver of Abaqus (Dassault System Simulia Corp, France). Steady-state Navier-Stokes equations were used to describe the flow problem. A velocity of 0.0125 m/s was applied to the inlet to ensure that fluid flow remained laminar throughout the scaffold, and an outlet pressure of 0 Pa was defined. A no-slip wall condition was set for the material/fluid interface areas. Water (density = 1000 kg/m<sup>3</sup> and viscosity = 0.001 Pa·s) was considered to be the working fluid. The average pressure at the inlet region was extracted to be used in Darcy's equation to determine the permeability coefficient.

### 2.5. Dynamic biodegradation tests

Dynamic *in vitro* biodegradation tests were conducted for up to 28 days in a custom-built bioreactor (Fig. 2b) using pre-equilibrated (5% CO<sub>2</sub>, 20% O<sub>2</sub>, 37 °C) revised simulated body fluid (r-SBF) [44] at a flow rate of 0.3 ml/min to mimic moderate physiological fluid movement in bone [45–47]. Upon removing specimens from the r-SBF solution, weight loss was determined after ultrasonic cleaning with 99% acetone and 96% ethanol, for 30 min each, and air-drying at room temperature (dry weight with an accuracy of 0.1 mg). Medium pH values (accuracy: ± 0.002) were registered after 28 days *in vitro* (InLab Expert Pro-ISM, METTLER TOLEDO). Concentrations of Fe, Ca, and P ions in the solution were analyzed using an inductively coupled plasma optical emission spectroscope (ICP-OES, iCAP 6500 Duo, Thermo Scientific).

### 2.6. Characterization of biodegradation products

Phase identification of the biodegradation products was performed using an X-ray diffractometer (XRD, Bruker D8 Advance

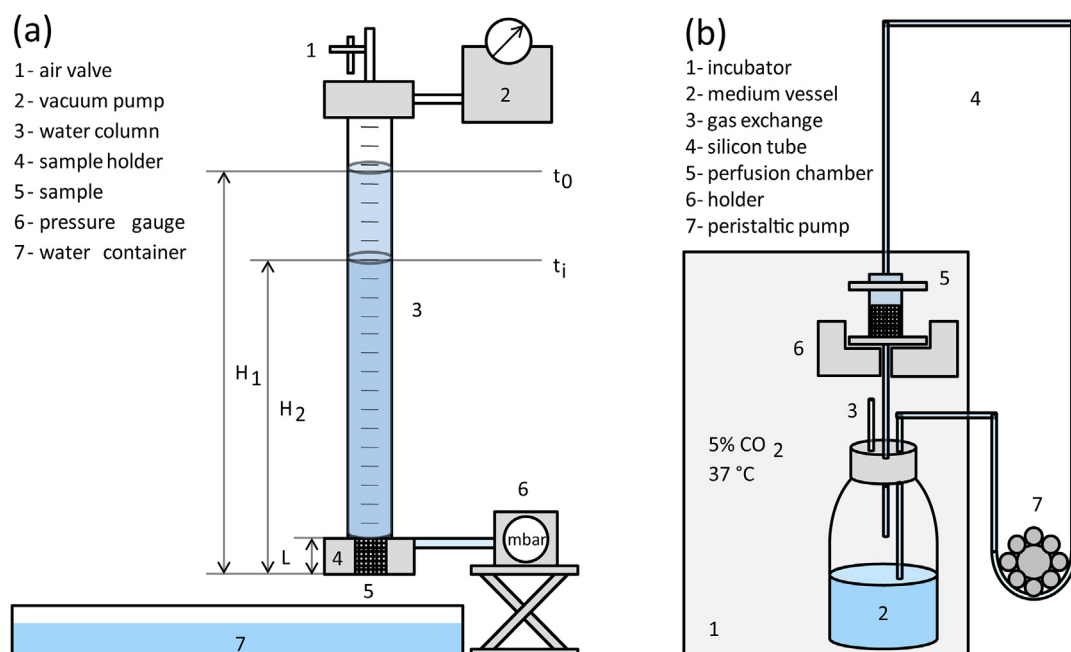


Fig. 2. Setups used for permeability measurements (a) and dynamic biodegradation tests (b).

diffractometer in Bragg-Brentano geometry). The diffractometer was equipped with a graphite monochromator and a Vantec position-sensitive detector and operated at 45 kV and 35 mA with a step size of 0.035° and a dwell time of 10 s per step using Co K $\alpha$  radiation. The morphologies and compositions of the biodegradation products on the surface of the specimens after the biodegradation tests were analyzed with a scanning electron microscope equipped with an energy-dispersive X-ray spectroscopy (EDS) (SEM, JSM-IT100, JEOL). In addition to observing the biodegradation products, the specimens were ultrasonically cleaned in ethanol and cut to observe the morphologies of the struts both at the periphery and in the center.

## 2.7. Mechanical characterization

Compression tests at a crosshead speed of 2 mm/min were carried out using an Instron mechanical testing machine equipped with a 10 kN load cell. The mechanical properties of the AM porous iron specimens before and after the biodegradation tests were determined according to ISO 13314:2011 and the quasi-elastic gradient (hereafter referred to as the elastic modulus) and yield strength were obtained. The elastic moduli of the porous structures were determined as the slope of the initial linear part of the stress-strain curve using linear fitting in the software Origin (OriginLab Corporation, USA). The initial linear part of the stress-strain curve was offset by 0.2% and its intersection with the stress-strain curve was taken to calculate the yield strength. The tests were performed in triplicate per specimen design and the mean values of the elastic modulus and yield strength were calculated as well as their standard deviations.

Simulations with the finite element method (FEM) were conducted using the commercial software package Abaqus (Dassault System Simulia Corp, France) to study the stress distributions in the specimens. Quarter-symmetric discretized models were built using a tetrahedron element (C3D10). The symmetry boundary conditions were defined on the longitudinal sections of the quarter-symmetric model. The top surface of the model was compressed to a displacement of 0.4 mm. The contours of the von Mises stress of the models were extracted to study the stress concentrations.

## 2.8. Cytocompatibility

The human osteoblast-like cell line MG-63 (ATCC, CRL-1427) was used for cytocompatibility analysis. Cells were cultured in Dulbecco's modified Eagle's medium with low glucose (100 mg/L, DMEM LG) (Sigma) with 10% fetal calf serum (PAN Biotech) (DMEM LG +) at 37 °C, 20% O $_2$ , 5% CO $_2$  and 95% humidity (physiological conditions). Cells were passaged at 80% confluency. After cleaning, all the scaffolds were sterilized for 30 min by immersion in 100% isopropanol (Merck; Darmstadt, Germany). All specimens were extracted at 37 °C for up to 72 h (EN ISO 10993-12 mod.) and extracts (10  $\times$ ) were compared to extracts (1  $\times$ ) from Ti6Al4V control scaffolds [34]. For cytotoxicity testing, extracts were sterile filtered (0.2  $\mu$ m) and the MTS assay was described in detail in our earlier publication [34], using Dimethyl sulfoxide (DMSO) (20%) as

positive control [48]. Two million MG-63 cells in 600  $\mu$ L DMEM LG were seeded per specimen. After 15 min, 10 ml of fresh DMEM LG+ was added and specimens incubated under physiological conditions for another 4 h. Cell-seeded scaffolds were then cut along their sagittal axis to access their central region and fluorescent staining was performed as described previously by us [34]. For SEM analysis, cell-seeded scaffolds were rinsed with 1  $\times$  phosphate buffered saline and fixed for 1 h in 3% glutaraldehyde (Agar Scientific, Wetzlar, Germany) in 0.1 M Soerensen's phosphate buffer (Merck, Darmstadt, Germany) at room temperature. Fixed scaffolds were dehydrated in 30, 50, 70, 90 and 100% ethanol, for 10 min each (last step twice). Samples were then air-dried at room temperature and the sagittal cut surface of the central region sputter-coated (Sputter Coater EM SCD500, Leica, Wetzlar, Germany) with 12.5 nm of gold-palladium and imaging at 10 kV in SEM (ESEM XL 30 FEG, FEI, Eindhoven, The Netherlands).

## 2.9. Statistical analysis

The optical density data (*i.e.*, MTS assay data) were normalized with respect to their corresponding controls. The obtained values of the relative cytotoxicity were then analyzed using a two-way ANOVA test ( $\alpha = 0.05$ ) followed by a post-hoc test (*i.e.*, Tukey's multiple comparisons test,  $\alpha = 0.05$ ). Statistical significance is indicated as  $p < 0.0001$ , \*\*\*\*;  $p < 0.001$ , \*\*\*;  $p < 0.01$ , \*\*;  $p < 0.05$ , \*; *n.s.* = not significant.

## 3. Results

### 3.1. Morphological characteristics

The porosity values measured by using micro-CT and weighing were similar to each other (Table 1). All the specimens had 6–9% less porosity than their nominal (*i.e.*, designed) values. As compared to the design values, the strut sizes were about  $\approx 50$   $\mu$ m larger and the pore sizes were  $\approx 50$   $\mu$ m smaller (Table 1). Reconstructed 3D models from micro-CT images confirmed that the strut thickness was radially graded for the specimens of the Dense-in and Dense-out groups, while the strut thickness remained uniform for the specimens of the S0.2 and S0.4 groups (Fig. 1c). The graded struts can be clearly observed in SEM image (Fig. S1).

### 3.2. Microstructure of the scaffolds

The AM iron had fine grains with an average size of  $12 \pm 0.3$   $\mu$ m (Fig. 3a) for the 0.4 m struts and  $10.8 \pm 1.4$   $\mu$ m for the 0.2 mm struts (Fig. 3b).

### 3.3. Permeability and velocity distribution

The order from the highest permeability of the AM iron specimens to the lowest was as follows: S0.2, S0.4, Dense-in, and Dense-out (Fig. 4a). Although the permeability values predicted by the CFD simulations were generally higher than the experimental results, they were well correlated to each other ( $R^2 = 0.84$ )

**Table 1**  
Topological characteristics of AM iron scaffolds.

AM iron scaffold	Strut size( $\mu$ m)		Pore size ( $\mu$ m)		Porosity (%)		
	Design	$\mu$ CT	Design	$\mu$ CT	Design	$\mu$ CT	Weight
S0.2	200	257 $\pm$ 3	800	755 $\pm$ 2	90.9	84.8 $\pm$ 0.1	84.6 $\pm$ 0.4
Dense-in	200–400	387 $\pm$ 1	800–600	609 $\pm$ 11	79.5	70.6 $\pm$ 0.4	69.7 $\pm$ 0.2
Dense-out	400–200	386 $\pm$ 5	600–800	635 $\pm$ 1	79.5	71.0 $\pm$ 0.2	70.3 $\pm$ 0.5
S0.4	400	461 $\pm$ 4	600	506 $\pm$ 11	67.0	58.4 $\pm$ 2.0	58.9 $\pm$ 0.3

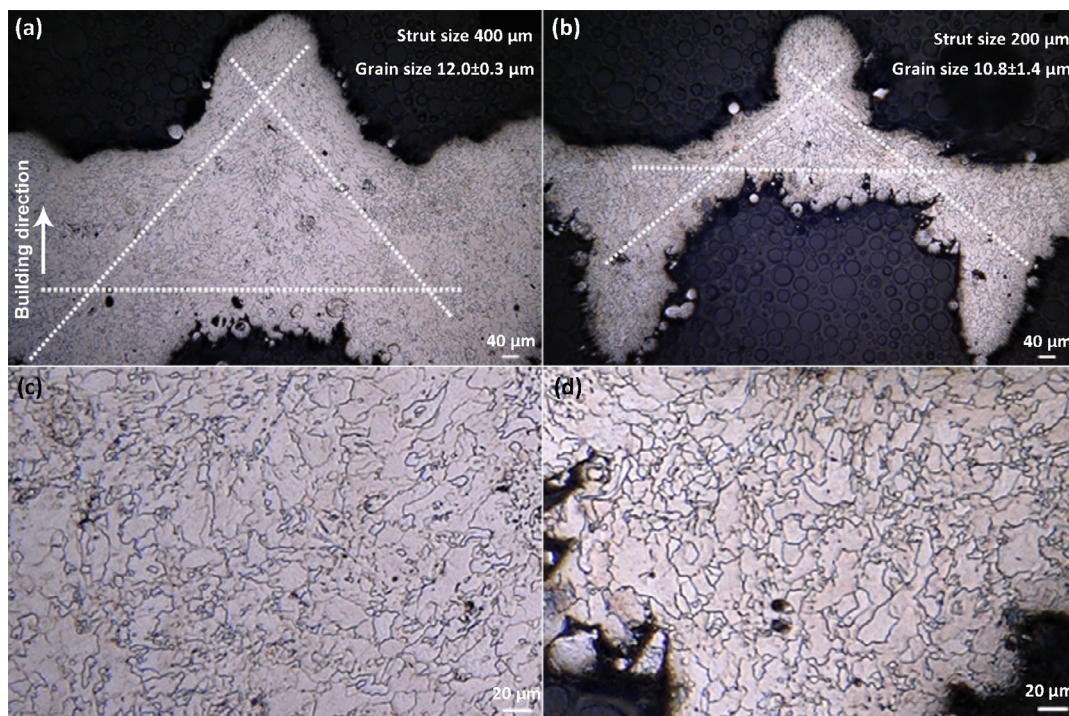


Fig. 3. Microstructures of the AM iron scaffolds with struts having a diameter of 400  $\mu\text{m}$  (a, c) and 200  $\mu\text{m}$  (b, d).

(Fig. 4b). The flow velocity distribution showed that the fluid velocity was homogeneous inside the specimens of the S0.2 and S0.4 groups (Fig. 4c). As for the functionally graded designs, the Dense-in specimens exhibited higher velocities at the periphery than at the center, while the opposite was true for the Dense-out specimens. Flow velocities values higher than the input velocity (*i.e.*, 0.0125 m/s) were also observed in the specimens (Fig. 4c).

### 3.4. In vitro dynamic biodegradation behavior

After 28 days of dynamic immersion, the pH values of the r-SBF solution increased marginally from 7.5 to around 7.6. There were no large differences between the pH values observed for the specimens of the different groups (Fig. 5a). The specimens of the S0.2 group exhibited a weight loss of  $16.7 \pm 3.3\%$ , which was the highest among all the experimental groups (Fig. 5b). The specimens of the group S0.4 had the lowest values of weight loss (*i.e.*,  $5.1 \pm 0.9\%$ ), which was about one-third of the maximum value (Fig. 5b). The weight loss of the specimens of the Dense-in and Dense-out groups lay between the extreme values, with the Dense-out specimens showing somewhat a higher value of weight loss (*i.e.*,  $10.3 \pm 0.3\%$ ) than the Dense-in specimens (*i.e.*,  $8.9 \pm 0.4\%$ ) (Fig. 5b). After normalizing the biodegradation rate by the surface area of the specimen, the ranking of the biodegradation rate was the same as that based on weight reduction (Fig. 5c). The specimens of the S0.2 group had a higher Fe ion concentration in the r-SBF than those of the S0.4 group, while the Dense-out specimens had a higher Fe ion concentration than the Dense-in ones (Fig. 5d). After 28 days, the concentrations of Ca and P ions decreased from the initial values of 100 mg/L and 31 mg/L, respectively, to around 50 mg/L and 10 mg/L, respectively (Fig. 5d).

### 3.5. Characterization of biodegradation products

Brownish biodegradation products accumulated on the surfaces of all the specimens after 28 days of biodegradation (Fig. 5e). The

biodegradation products contained lepidocrocite [*i.e.*,  $\gamma\text{-FeO(OH)}$ ] and goethite [*i.e.*,  $\alpha\text{-FeO(OH)}$ ] (Fig. 5f). However, the intensity peaks of these biodegradation products in the XRD patterns were relatively low. SEM analysis of external struts showed that, after 28 days of immersion, two types of biodegradation products were formed on the surface: grey earth-cracking-like layers at the bottom and pockets of white loose compounds on the top (Fig. 6). EDS analysis indicated that the grey biodegradation products contained C, O, and Fe, while the white biodegradation products contained P, Ca (Fig. 6), and sometimes Na (Fig. 6b). Different biodegradation behaviors were observed from the center to the periphery of the specimens (Fig. 7). After disintegrated degradation products on the struts were removed, the grain boundaries became clearly visible. In the case of the specimens from the S0.2, S0.4, and Dense-in groups, the grain structure turned out to be better definable on the periphery of the specimens (Fig. 7a, c, and g) than in their center (Fig. 7b, d, and h). Moreover, the center of all the specimens contained some remnants of the biodegradation products even after cleaning (Fig. 7b, d, f, h). We further assessed the volume losses of the specimens in the center using micro-CT and found that the Dense-out specimens had a larger weight reduction than the S0.2 specimens, even though their geometry were exactly the same in the center (Fig. 7i). The specimens of the S0.4 group degraded faster than the Dense-in specimens, although they had the same geometry in the center (Fig. 7i).

### 3.6. Mechanical properties

Under uniaxial compression, all the specimens exhibited smooth stress-strain curves without sudden fluctuations after yielding, both before (Fig. 8a) and after (Fig. 8b) biodegradation tests. All the stress-strain curves followed similar patterns, starting with a linear elastic region and continuing with a rapidly decreasing slope until a plateau stage with almost no fluctuations was reached (Fig. 8a, b). A densification phase ultimately resulted in a rapid increase in stress (Fig. 8a, b). Among all the experimental

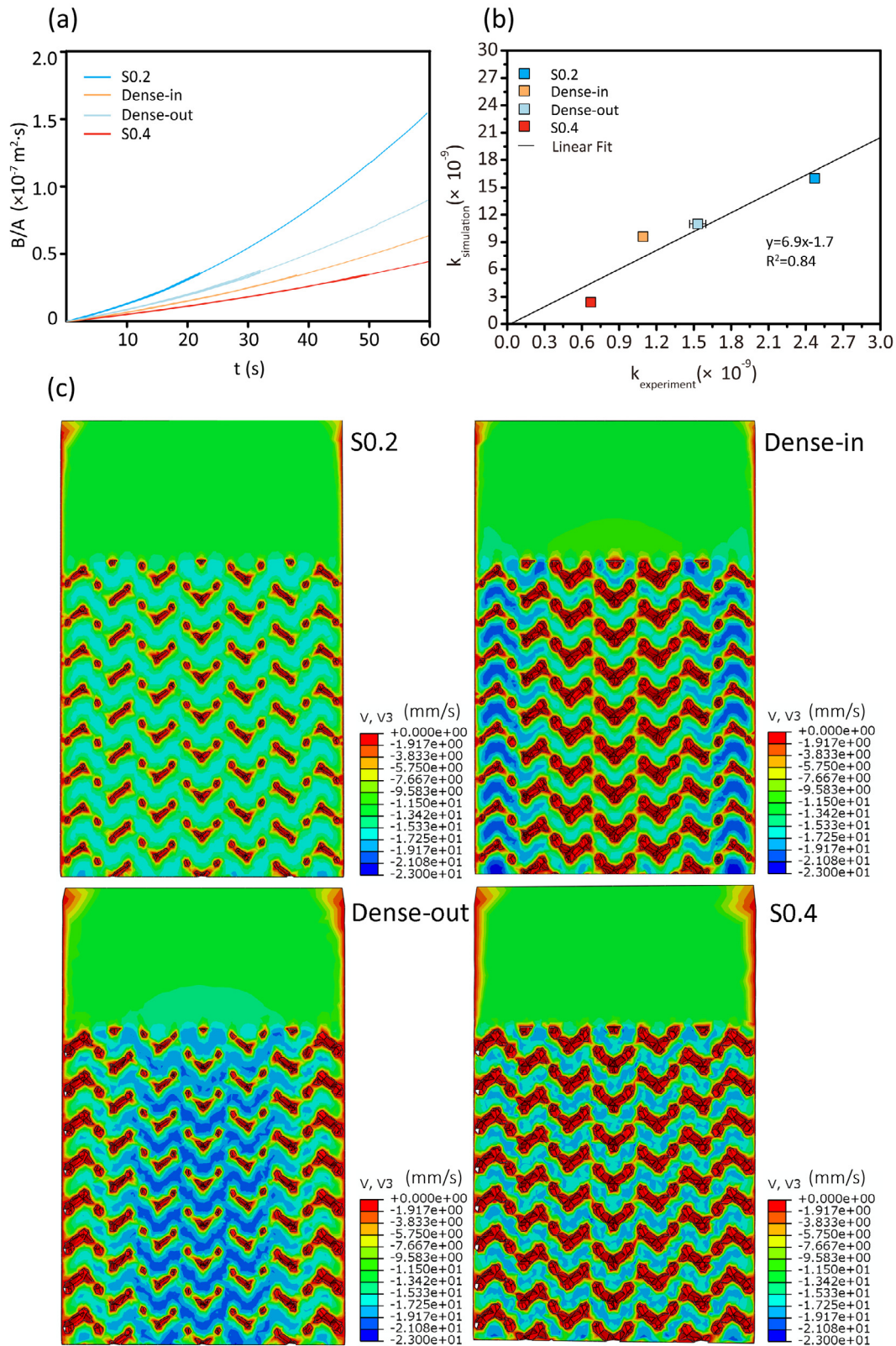


**Fig. 4.** Results from the permeability tests and CFD simulations of the AM porous iron scaffolds with the different topological designs: experimental results (a), permeability values (b), and velocity distributions predicted by the CFD models (c).

groups, the S0.4 group possessed the largest values of yield strength ( $53.1 \pm 0.9$  MPa) and elastic modulus ( $2815.9 \pm 126.6$  MPa), while the S0.2 group exhibited the lowest

values of yield strength ( $10.7 \pm 0.4$  MPa) and elastic modulus ( $891.6 \pm 89.7$  MPa) (Fig. 8c, d). The mechanical properties of the functionally graded groups fell between those of the S0.4 and

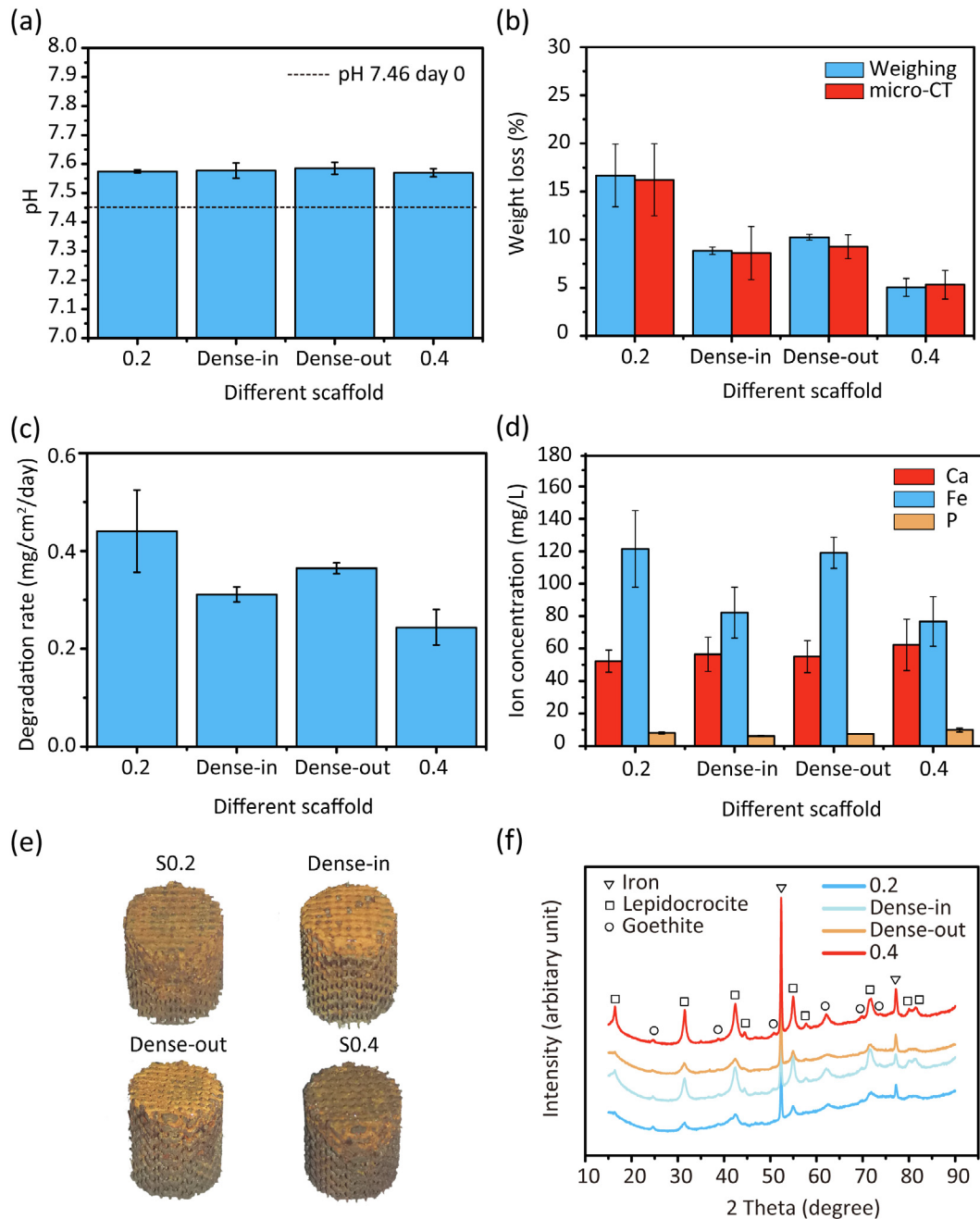


**Fig. 5.** Results from the dynamic biodegradation tests for 28 days: pH value (a), weight loss (b), biodegradation rate (c), ion concentration (d), the appearance of the specimens (e), and XRD patterns (f).

S0.2 groups (Fig. 8c, d). The Dense-in scaffolds had somewhat higher values of yield strength ( $32.9 \pm 1.6$  MPa) and elastic modulus ( $1767.3 \pm 48.5$  MPa) than the Dense-out specimens ( $30.5 \pm 0.3$  MPa &  $1754.4 \pm 30.8$  MPa) (Fig. 8c, d). Yield strengths and elastic moduli of all the specimens decreased after 4 weeks of biodegradation (Fig. 8c, d).

FEM simulations showed that von Mises stresses were uniformly distributed in the S0.2 and S0.4 specimens (Fig. 9), while the Dense-in and Dense-out specimens had more stress concentrations in their thicker struts. Moreover, at the same level of displacement, the Dense-in and Dense-out specimens showed lower values of the maximum von Mises stress than those observed for the S0.2 and S0.4 specimens.

### 3.7. Cytocompatibility

To evaluate the potential of AM porous pure iron specimens for biomedical applications, we performed biocompatibility testing (Fig. 10). Relative cellular activity of human osteoblast-like MG-63 cells in extracts from the different types of iron scaffolds (a-d) was compared to that of control extracts from bio-inert Ti-6Al-4V. Cell viable in 24 h-extracts was  $> 75\%$  for all iron specimens, independent of their structural differences: 77.8% (S0.2), 79.2% (Dense-in), 82.2% (Dense-out) and 86.5% (S0.4). Interestingly, while the cell viability in extracts from other specimen types gradually decreased in an extraction time-dependent manner, cell viability in S0.4 extracts remained at almost 70% even after 48 h of

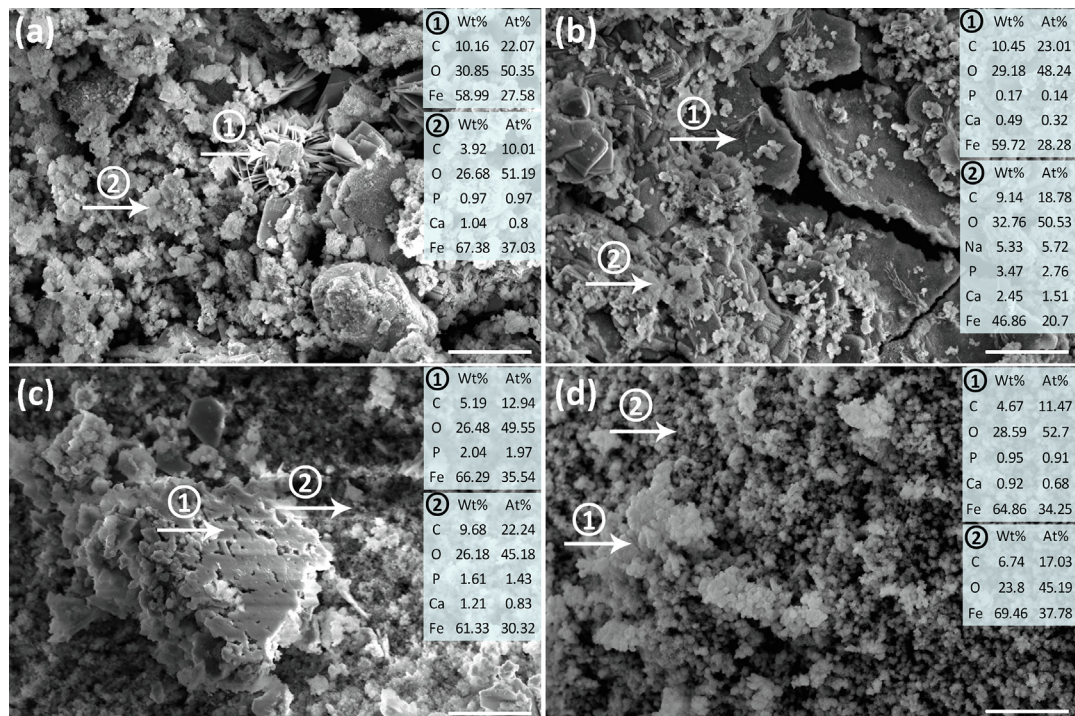


**Fig. 6.** Morphologies and chemical compositions of the biodegradation products formed on the AM porous iron specimens after 28 days: (a) S0.2 (b) Dense-in (c) Dense-out, and (d) S0.4. Scale bar: 10  $\mu\text{m}$ .

extraction and did not significantly differ from Ti-6Al-4 V controls (Fig. 10d). MG-63 viability in extended, long-term extracts (72 h) of iron specimens dropped to below 50%, while Ti-6Al-4 V extracts did not reveal significant cytotoxicity.

Direct cytocompatibility assessment revealed fluorescently labeled adhered cells at the periphery as well as in the center of the scaffolds. However, when comparing specimens of the different groups no design-specific cell distribution pattern could be identified (Fig. 10e). Gradients in strut thickness (*i.e.*, dense-in vs. dense-out) did not obviously influence regional cell seeding density. SEM images of MG-63 cells, 24 h after seeding, revealed a well-spread polygonal cell morphology with cytoplasmic projections attached to the surfaces of the iron scaffolds (Fig. 10f, box).

#### 4. Discussion

AM porous metallic biomaterials should meet multiple contradictory design criteria that are often difficult to reconcile without sacrificing one or the other to some extent. Here, we report for the first time how functional gradients can be used to meet these design requirements through directly printing a biodegradable porous iron biomaterial. The biodegradation of iron *in vivo* is generally slow, meaning that we should try to exploit topological design to increase the biodegradation rate of AM porous iron while ensuring sufficient mechanical support and proper nutrient transport. Our results clearly show that with the aid of topological design ideas in general and functional gradients in particular, the biodegradation rate and mass transport properties (*i.e.*, permeability) of AM porous iron can be increased while maintaining the bone-mimicking mechanical properties of these biomaterials.

##### 4.1. Morphology and microstructure

All the topological designs of porous iron could be directly printed with the morphological parameters that were close to

the design values. Due to thickened struts, the actual porosities were slightly lower than the design values for all the groups. As a strut thickness of 200  $\mu\text{m}$  is quite thin, the actual strut diameter was nearly 60  $\mu\text{m}$  larger than the design value, even when the contour scanning strategy was used. On the other hand, under the printing conditions used, the reproducibility of the scaffolds was high (with a standard deviation of 5% or lower).

As to the microstructure, micro melt pools formed during SLM [49], leading to high cooling rates ( $10^3$ – $10^8$  K/s) [50], which resulted in a non-equilibrium solidification process and refined grains (*i.e.*, 10–12  $\mu\text{m}$ , in this study). As no large differences between the grain sizes of thick and thin struts were found, the different biodegradation behaviors of the different experimental groups were unlikely caused by their microstructures, but rather by their porous architectural features. Moreover, unlike previously reported AM solid iron [51,52], our AM porous iron specimens did not exhibit obvious elongated grains along the build direction, which can also be seen by Electron Back-Scattered Diffraction (EBSD) analysis in our former paper [38]. This suggests that the effects of any directional solidification processes were not as strong as in the case of solid counterparts, particularly given that the struts of our scaffolds were built in a tilted orientation. The reason for this could be that there was limited overlap between the melt pools of different layers during the SLM process when the strut was tilted (Fig. S2).

##### 4.2. Permeability

As expected, permeability was highly dependent on the porosity of the specimen and influenced by porosity distribution on the transverse section. According to the Kozeny-Carman equation, the relationship between the permeability,  $k$ , porosity,  $\phi$ , and the specific surface area,  $S_v$ , (*i.e.*, surface to volume ratio) of a porous structure is given by:  $k = C_K \phi^3 / S_v^2$ , where  $C_K$  is an empirical constant [53]. A higher porosity, therefore, results in a much higher

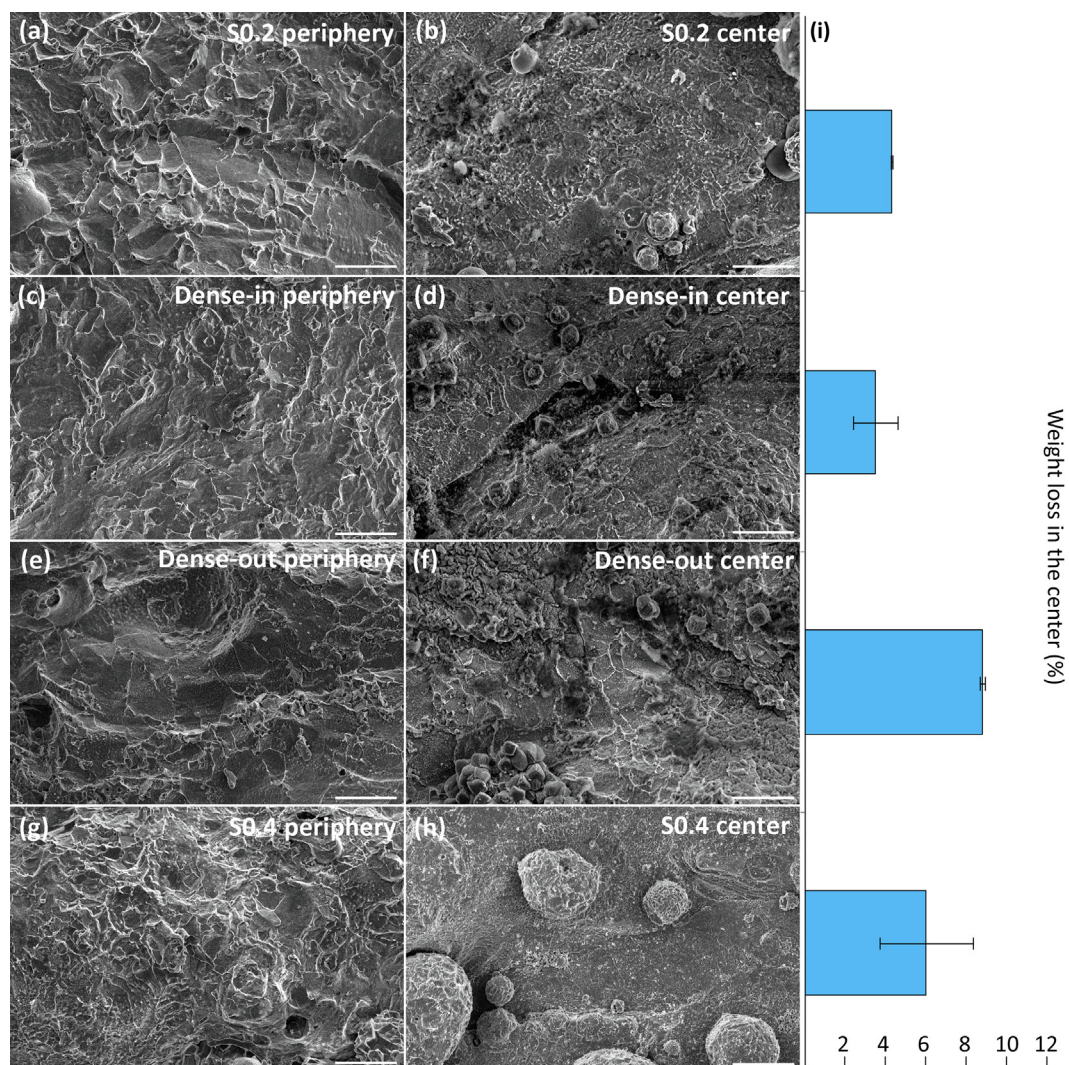


**Fig. 7.** Morphologies of the biodegraded AM porous iron specimens after cleaning on the periphery (left) and in the center (right): S0.2 (a, b), Dense-in group (c, d), Dense-out group (e, f), S0.4 group (g, h), and the weight losses of the specimens of the different groups in the center (i) after immersion for 28 days. Scale bar: 10  $\mu\text{m}$ .

permeability value. Interestingly, although the functionally graded Dense-in and Dense-out specimens had similar overall porosities, the Dense-out specimens showed higher permeability values than those of the Dense-in group. This may be due to the different  $C_K$  values for these two structures, as  $C_K$  is strongly dependent on pore geometry [54]. It may thus be concluded that, in addition to porosity, permeability can be also adjusted through topological design and the spatial distribution of repeating unit cells.

CFD simulations could help us to reveal the flow behavior of the scaffolds. Although the permeability values calculated from the simulations were higher than the experimental values, they were well correlated to each other (Fig. 4b). The discrepancies between the measured and predicted values could be attributed to the following factors. First, the CAD models had lower porosity and surface roughness than the actual values of the AM iron specimens. These differences might have caused an overestimation of the permeability. Furthermore, as can be seen from the velocity distribution (Fig. 4c), even though we chose a slow inlet velocity, the actual velocity inside the scaffolds could be higher, which means that turbulent flow might occur. This phenomenon has also been observed by other researchers and appears to be caused by obstacles on the fluid path [55]. Turbulent flow might decrease the permeability of the scaffolds during the tests. It was also interesting to observe

how the geometry could guide the flow behavior in the functionally graded scaffolds. For the Dense-in and Dense-out specimens, the higher porosity region always had a higher flow velocity (Fig. 4c). A higher flow velocity can facilitate nutrient and oxygen transport to the cells residing inside the center of a scaffold [56].

#### 4.3. Biodegradation behavior

The weight losses of the specimens were strongly dependent on their topological designs. Optimizing the topological design of the porous structure could, therefore, be an effective means to adjust the biodegradation behavior of AM porous iron. In general, the higher the porosity, the faster the weight loss. Furthermore, as the specimens from the different groups had different surface areas, we normalized the biodegradation rate to the surface area. The ranking of the different experimental groups in terms of biodegradation rate remained the same with or without normalization. As the biodegradation rate is directly related to the fluid flow inside the porous structure, topological design may influence the biodegradation behavior of AM iron scaffolds also through its effects on fluid velocity and permeability (subsection 4.2).

Visual inspection revealed that under dynamic biodegradation, brownish corrosion products formed both at the periphery and in

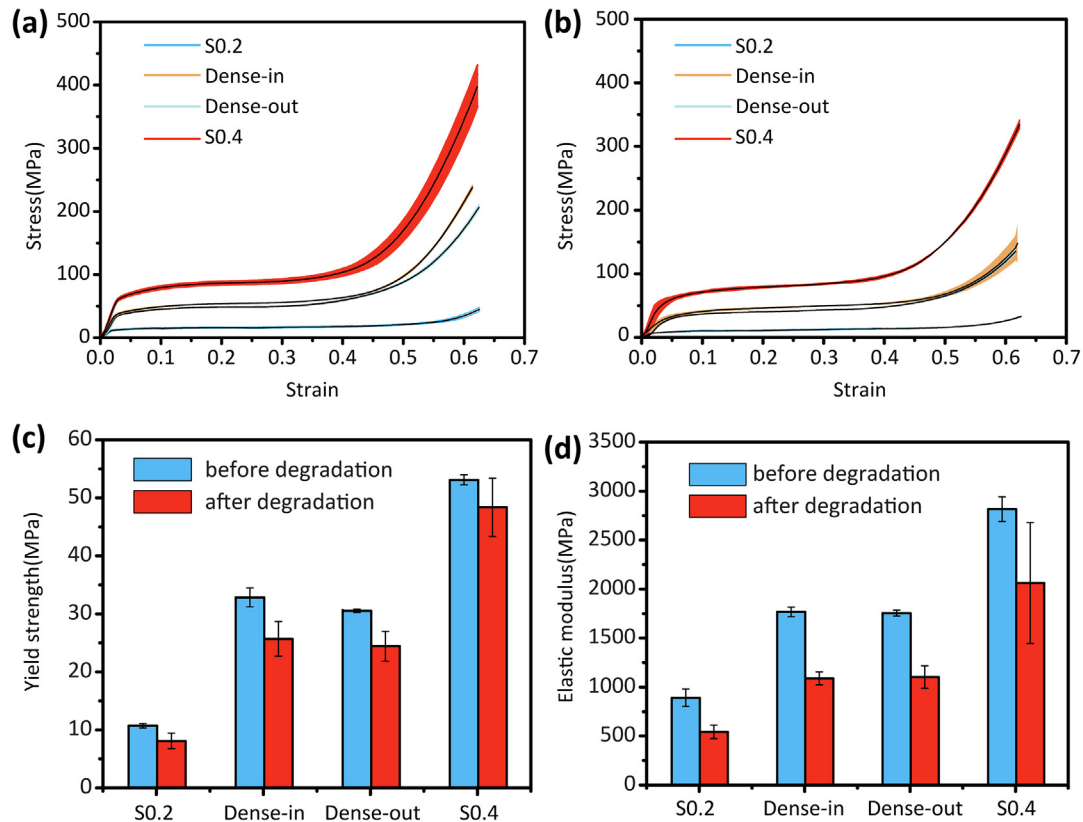


**Fig. 8.** Mechanical properties of the AM porous iron specimens before and after biodegradation for 28 days: (a) stress-strain curves before biodegradation, (b) stress-strain curves after biodegradation, (c) yield strengths, and (d) elastic moduli.

the center of the specimens (Fig. 5). EDS analysis indicated that the corrosion layer of the external struts contained Ca and P elements (Fig. 6) after 28 days of immersion. Combined with ICP results (Fig. 5d), these observations suggested that the Ca and P elements on the corrosion layer originated from the r-SBF medium. To better understand the different biodegradation mechanisms, we inspected the surface morphologies of degraded struts after ultrasonic cleaning (Fig. 7). Biodegradation occurred both at the periphery and in the center of the specimens and grain boundaries became clearly visible on the surfaces of the struts (Fig. 7). This was different from our previous study on ‘uniform’ AM porous iron, where struts in the center of the specimens remained almost intact after 28 days of immersion [34]. It could be explained by dynamic flow. In order to find out how topological design could be used to adjust the biodegradation behavior of the AM iron scaffolds, the central regions of the AM iron specimens were inspected by micro-CT. Although the specimens of the S0.2 and Dense-out groups had exactly the same geometry in the center (Fig. 1), the weight loss of the Dense-out specimens in the center was higher than that of the S0.2 specimens. This is counter-intuitive, given that the S0.2 specimens had higher permeability values than the specimens of the Dense-out group (Fig. 7i). However, the velocity distribution predicted by CFD simulations (Fig. 4c) suggests that the Dense-out scaffolds had higher flow velocities in the center than on the periphery. As the inlet flow velocity was constant in our dynamic biodegradation tests, there was a higher medium volume flow in the center of the Dense-out specimens. Similar results were observed for the S0.4 and Dense-in specimens. The Dense-out specimens degraded more slowly than the S0.4 specimens in the center, although the Dense-out specimens had generally higher permeability values than the S0.4 group. Once again, velocity distribution of the Dense-in specimens showed that the fluid velocity

was higher at the periphery than in the center, leading to less medium volume flowing through the center of these specimens.

After 28 days of dynamic immersion, all the specimens lost more weight (*i.e.*, 5–16%) than the ‘uniform’ AM iron scaffolds under static immersion conditions (*i.e.*, 3%) used in our earlier study [34]. It is well known that the *in vitro* test environment can affect the biodegradation rate of biodegradable metals. Others reported higher biodegradation rates of iron in dynamic immersion tests [57] as well. Furthermore, maintaining the CO<sub>2</sub> content at 5% means that the pH of the medium remains constant around 7.6. This would increase the biodegradation rate as well. The human body is a buffered system with a pH range of 7.38–7.42 [58]. Moreover, a flow rate of 0.012–1.67 ml/min [59] continuously occurs inside the (intra) medullary cavities that are home to the bone marrow and the progenitor cells of osteoblasts and osteoclasts. The dynamic biodegradation setup used in this research can, therefore, better mimic the *in vivo* conditions.

The biodegradation rates of the AM porous iron scaffolds observed here are higher than those reported for the pure iron fabricated using conventional manufacturing techniques (*i.e.*, 0.04–0.06 mg/cm<sup>2</sup>/day<sup>-1</sup>) [48,57], similar to those of cross-rolled pure iron (*i.e.*, 0.24–0.29 mg/cm<sup>2</sup>/day<sup>-1</sup> [60]), and lower than those of electroformed pure iron (*i.e.*, 1.39 mg/cm<sup>2</sup>/day<sup>-1</sup> [61,62]). This is consistent with the order of the grain sizes obtained from using these different fabrication techniques. Conventionally manufactured iron has grain sizes in a range of 180–400 μm [48,57], while the grain sizes of cross-rolled and electroformed iron are 16–19 μm [60] and 4 μm [61,62], respectively. The AM porous iron specimens printed here had an average grain size of 10–12 μm, which is close to that of cross-rolled iron. Indeed, the specific solidification process experienced during AM creates smaller grains, which in turn increases the grain boundary area with defects in the crystal

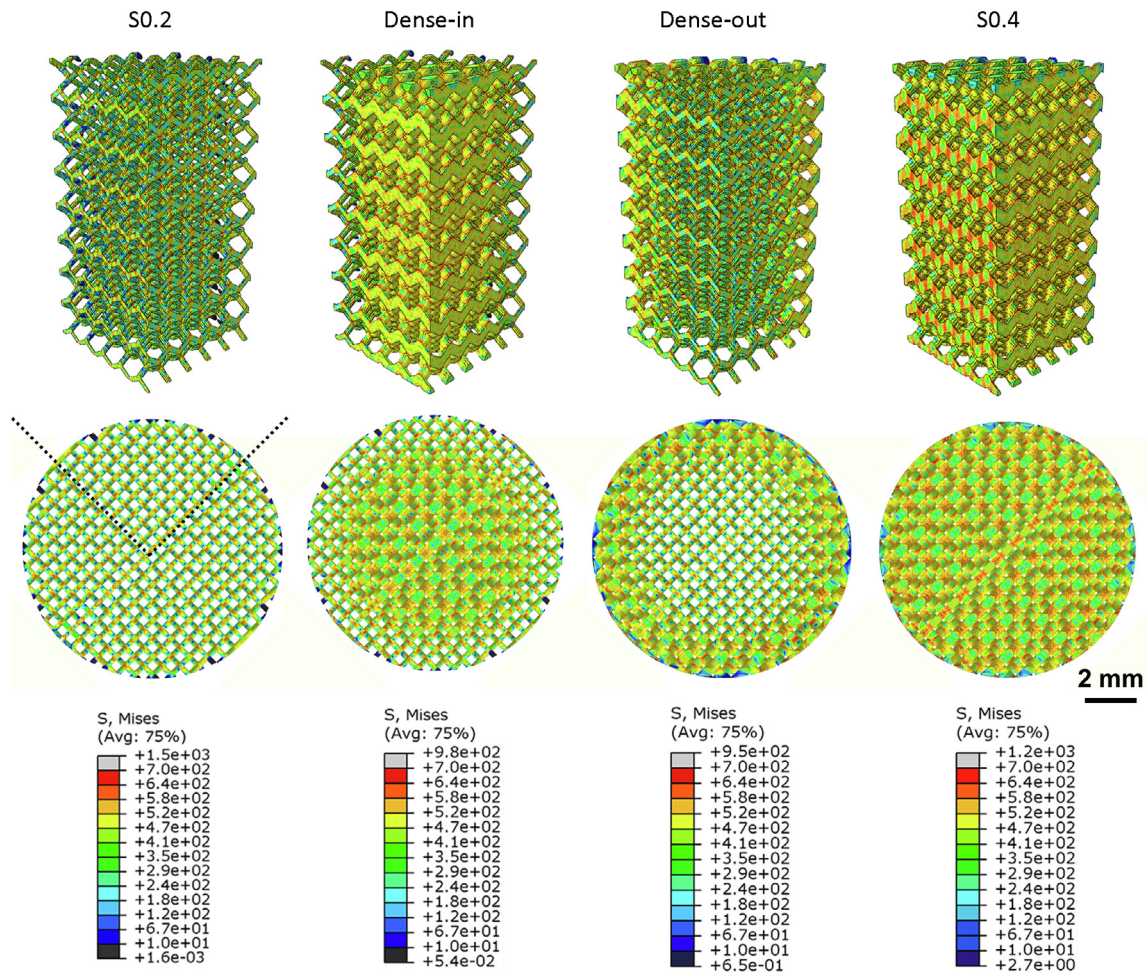


Fig. 9. Distributions of the von Mises stress in the AM porous iron specimens at 0.4 mm displacement under compression predicted by FE modeling.

structure and high internal energy [63]. Larger areas of grain boundary are expected to cause higher chemical activity in a corrosive medium [64,65]. This clearly shows the advantage of the refined microstructure resulting from the SLM process in increasing the biodegradation rate of slowly degrading metals such as iron. Of course, other microstructural features such as texture and dislocation density may also affect the corrosion rate [60].

The actual weight reduction could be even higher than those measured here, because usual sample cleaning methods and weight loss measurements for solid samples cannot easily be applied to a porous specimen. For solid specimens, it is feasible to remove all the corrosion products with minimum attack to the sample itself. In the case of highly porous scaffolds, however, it is difficult to remove all the corrosion products, especially those in the center of the specimens (Fig. 7b, d, f, h). Others have used acids or alkalis to remove corrosion products [66–69], but this may result in further erosion of the struts, particularly at the periphery. ICP-OES analysis showed even less iron release into the r-SBF medium as compared to the expectation from the weight loss measurements. This might be because iron ions participated in the formation of corrosion products (EDS results, Fig. 6).

Although AM porous irons showed a sufficient rate of biodegradation in this study that should result in full biodegradation of the specimens within 1–2 years [68], the *in vivo* tests of AM porous iron should be performed in the future. In the case of bulk iron, a number of animal studies have shown that the *in vivo* degradation rates may be significantly lower than those measured *in vitro* [38,39,69]. It is, therefore, of great interest to determine the

biodegradation rate of AM porous iron *in vivo* to better determine the potential of these biomaterials for future clinical application.

#### 4.4. Mechanical behavior

The mechanical properties of all the AM porous iron specimens remained within the range of values reported for trabecular bone (*i.e.*,  $E = 0.5\text{--}20$  GPa [70],  $\sigma_y = 0.2\text{--}80$  MPa [71]) even after 28 days of biodegradation. Unlike other AM porous structures based on a diamond unit cell that were made from other materials [11,72], the AM porous iron specimens studied here showed smooth stress-strain curves during uniaxial compression tests without fluctuations after the maximum stress (Fig. 8a). In addition, no sudden failures occurred. This could be explained by the high ductility of pure iron [34]. Similar behavior has been observed for other highly ductile porous materials, such as AM porous structures made of pure titanium and tantalum [12,73]. In the case of the functionally graded designs, the shape of the struts gradually and continuously changed so as to minimize the discontinuity of the stress at the interface between dissimilar layers [24]. The stress-strain curves remained smooth after the *in vitro* immersion tests and showed similar patterns to those of the non-biodegraded specimens (Fig. 8b). Among the different designs, the yield strengths and elastic moduli of the AM iron specimens were strongly affected by porosity: a higher porosity resulted in lower values of yield strength and elastic modulus. The mechanical properties of functionally graded structures could be predicted, based on the weighted average of the mechanical properties of each constituent

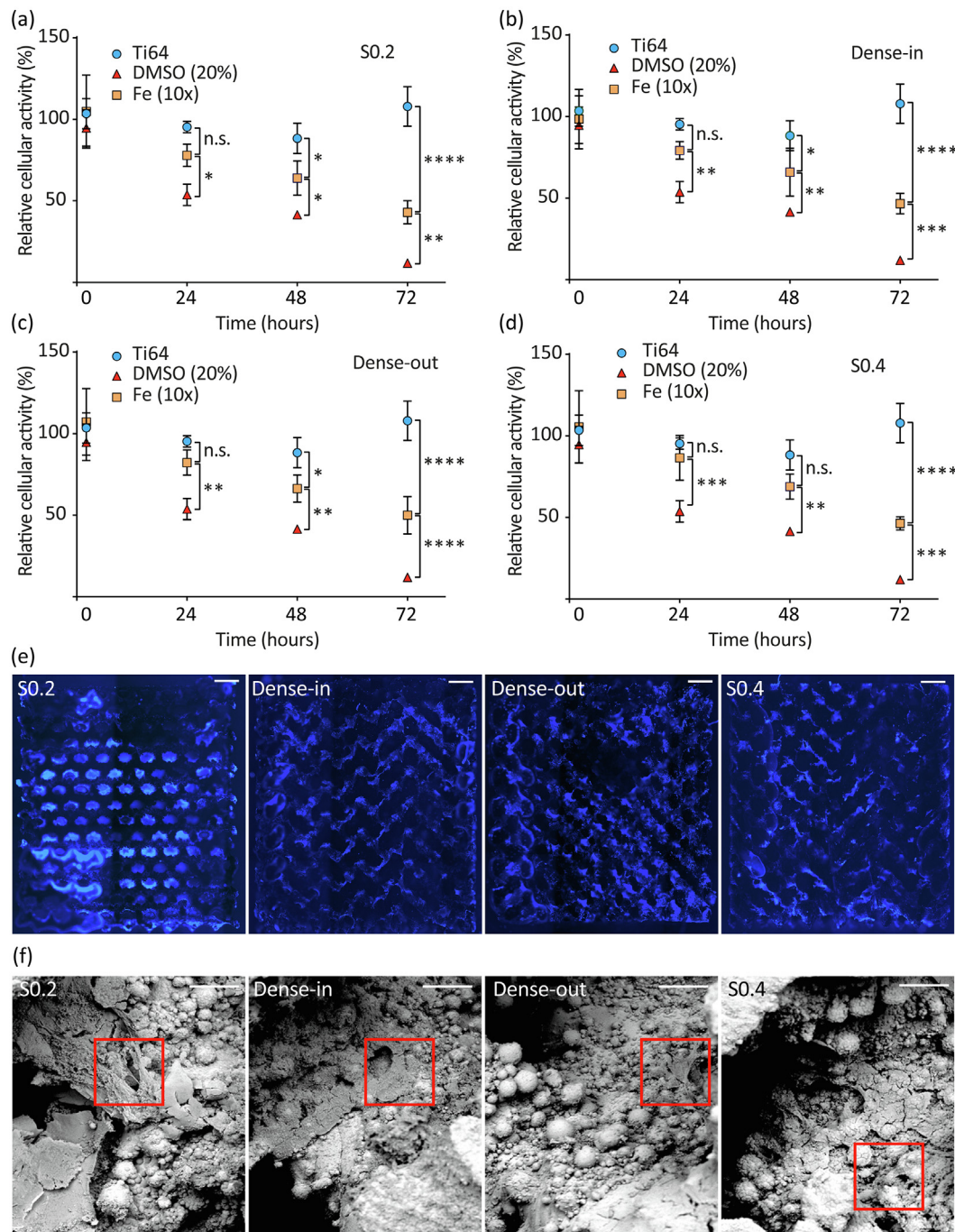


**Fig. 10.** Cell distribution and cytocompatibility. Relative cytocompatibility (%) of different groups of iron specimens was assessed against titanium controls: S0.2 group (a), Dense-in group (b), Dense-out group (c), and S0.4 group (d). Fluorescently stained MG-63 cells on different AM porous iron specimens (e), and SEM analysis (f), respectively. Scale bar: 1 mm (e) and 100 μm (f). Experiments were performed with extracts of randomly chosen replicate iron specimens (yellow squares,  $n = 5$ ) and compared to AM Ti-6Al-4V scaffolds (blue circles, Ti64;  $n = 3$ ) of the same design ( $n = 3$ ) as positive controls and to dimethylsulfoxide (DMSO, red triangles) as negative controls. *n.s.*, not significant; \*,  $p < 0.05$ ; \*\*,  $p < 0.01$ ; \*\*\*,  $p < 0.001$ ; \*\*\*\*,  $p < 0.0001$ . (For interpretation of the references to colour in this figure legend, the reader is referred to the web version of this article.)

using the Voigt model [21]. Based on this model, the elastic modulus and strength of the functionally graded scaffolds are given by:  $P_g = \sum_{i=1}^n f_i P_i$ , where  $P_g$  represents the elastic modulus or strength of the functionally graded structure and  $f_i$  is the volume fraction of  $P_i$ . However, we find that such a weighted average cannot fully predict the mechanical properties of the functionally graded specimens designed in this study. For example, even though the Dense-in and Dense-out groups had similar porosities, both the yield strength and elastic modulus of the Dense-in specimens were

slightly higher than those of the Dense-out group. The results from FE modeling of the specimens under compression could explain this trend. Given that stress was more concentrated in thicker struts, they carried more loads than thinner ones. Although both functionally graded groups had similar porosities (*i.e.*, the same volume of thick struts), the thickest struts were located at the periphery of the Dense-out group specimens, meaning that the thickest struts were generally open (*i.e.*, dangling) and did not contribute to the load-bearing capacity of the specimens.

Functionally graded structures have been reported to exhibit better failure performance than their uniform counterparts. For example, an axisymmetric deformation mechanism and long plateau stage have been observed for functionally graded specimens during compression tests, instead of abrupt failure accompanied by shear band formation [21,24–26]. As thicker struts are the primary load-bearing elements of functionally graded structures, deformation occurs primarily in these struts, resulting in trumpet-like specimens after compression [21]. Functional gradients have been also found to increase the fatigue resistance of AM porous structure [25], as the cracks initiate layer by layer, instead of randomly initiating everywhere in the scaffolds at the same time. However, the results available for functionally graded AM porous metallic biomaterials in the literature usually refer to Ti-6Al-4V, which is a brittle alloy if no post-AM treatment is performed. As we used pure iron here, functional gradients did not alter the failure mode of the AM iron scaffolds, as the uniform designs exhibited smooth stress-strain curves themselves.

The structure of the human bone is generally highly heterogeneous and anisotropic with different stiffness and strength values in different directions [4]. At the same time, bone has sufficient permeability to facilitate the transfer of cells and nutrients. Bone-substituting porous implants should, therefore, combine a tailor-made distribution of mechanical properties with certain ranges of permeability, while taking biodegradation into account. The designs that we used in this study attempted to achieve these goals to the extent that was possible with linearly and radially graded porous structures. Of course, to fully address the above-mentioned design criteria regarding the mechanical, physical, and biological properties, further research attempts are needed. Topological optimization may be used to aid in achieving the desired properties while satisfying certain prescribed constraints. Indeed, Hollister [74,75] has advocated the adjustment of both stiffness and diffusive transport properties using topology optimization when designing scaffolds.

#### 4.5. Cytocompatibility

To evaluate the biomedical application potential of our novel AM porous pure iron specimens, we applied latest ISO 10,993 modifications to meet the special requirements for absorbable biomaterials [76,77]. To this end, we used an MTS assay, which is the current state-of-the-art for extract-based *in vitro* evaluation of cytotoxicity [78]. In addition, using a medium containing serum allows to extract both polar and non-polar substances and supports cellular growth (ISO 10993-5, 2009) [78]. Of note, within the physiological range of 37 °C, 24 h and 72 h are both specifically acceptable extraction conditions according to ISO 10993 (2009), with 72 h being the relatively harsher extraction regime [78]. Accordingly, in 24 h-extracts, cell activities in all iron extracts ranged between 77.8% (S0.2, the lowest) and 86.5% (S0.4, the highest), respectively, and can be classified as non-cytotoxic (*i.e.*, cytotoxicity grade 1; 75–99% viability) [79]. Upon 48 h-extraction, all conditioned media revealed  $\geq 63\%$  remaining cellular activity, corresponding to being slightly cytotoxic (*i.e.*, grade 2, 50–74%). Of note, under these conditions, the S0.4 group was still not significantly more cytotoxic than the titanium control, while Ti-6Al-4V controls remained non-toxic (grade 1) throughout. Only upon harsh 72 h-extractions, 75% of the samples have to be classified as moderately cytotoxic (*i.e.*, grade 3, < 49%). In line with our data, cytotoxicity was earlier reported to be inversely proportional to the iron ion concentration [66,80]. Iron is an essential transition metal and nutritional requirement in cell culture, having both beneficial and toxic properties. The loss of ferric iron due to precipitation and its reduction to ferrous iron are equally undesirable events in the extracellular milieu. Ferric iron is the stable oxidative

state of iron in aerobic conditions, and the normal oxidative state used by cells. In a solution at physiologic pH, ferric iron that is not bound by a chelator or carrier molecule will form ferric hydroxide complexes that are virtually insoluble. While the chemistry is quite complex, ferric iron can be reduced to ferrous iron which is free to participate in Fenton chemistry, to become a major source of oxidative stress in media due to the creation of hydroxyl free radical [81]. Pure iron showed good biocompatibility during long term implantation as biodegradable stents or pins [40,41,82,83], which is in agreement with our *in vitro* results using the mild extraction regime. Unlike the *in vitro* situation where released iron ions can accumulate locally to high concentrations in a culture dish, released ions are usually rapidly diluted *in vivo* and will ultimately be secreted from the body [84]. This difference may point towards important limitations of the currently used static methods to evaluate cytocompatibility as they may tend to overestimate cytotoxic effects.

Fluorescent staining revealed relatively uniform cell seeding throughout the iron scaffolds without apparent design-specific differences (Fig. 10e). This is in agreement with a recent study where human mesenchymal stromal cells were analyzed in 3D scaffolds with gradient pore sizes [85] and a study using pre-osteoblasts in gradient Ti-6Al-4V scaffolds [27]. The latter authors concluded that the degree of cell attachment was similar for various strut thicknesses. However, we expected that relatively more cell would adhere to thicker struts as compared to thinner ones, as these struts provide larger surface area to cells (and thus interfacial force). Logically, this might lead to more interactions with the material surface before the cells slip through the pores [22,59]. Our analyses of cell distribution between Dense-In and Dense-Out groups did not reveal obvious differences in support of this former notion. Of note, our iron specimens were spatially graded instead of axially graded along the z-axis, as reported by others [20,22,23]. Axially grading could result in “sieve effects” during cell seeding and may account for differences between the studies. In addition, fluorescent labeling in porous, but otherwise light-dense, 3D structures has some limitations: subtle differences in cell distribution were hard to quantify due to large quantities of interfering iron biodegradation products. Such artefacts are absent in titanium scaffolds, facilitating quantification when using inert materials. Furthermore, the minimum and maximum pore sizes of our gradient scaffolds were 0.6 mm and 0.8 mm, respectively. This difference may not be large enough to affect cell seeding and qualifying both types as scaffolds of higher porosity [13]. Altogether, this may explain why we observed a rather uniform distribution in our gradient and non-gradient scaffolds. However, further decreasing the minimum pore size in smartly designed functionally graded porous scaffolds might hold potential to control cell distribution.

#### 5. Conclusions

We demonstrated for the first time how SLM could be used for direct printing of functionally graded porous iron. The specimens of all the groups (*i.e.*, two functionally graded groups and two uniform groups) possessed precisely controlled topologies and fully interconnected porous structures. The topological design not only affected the permeability of the specimens of these groups but also changed the fluid flow inside the specimens. Consequently, the topological design controlled the biodegradation behavior of the AM porous iron scaffolds. For example, different biodegradation rates were found in the center of the AM porous iron specimens with and without functional gradients, even though they had the same local geometry. Taken together, our results suggest that topological design in general, and functional gradients in particular can

be used as an important tool for adjusting the biodegradation behavior of AM porous metallic biomaterials. This holds especially for otherwise slowly degrading metals, such as iron, to reach values desired for bone substitutes. Over a period of 28 days of dynamic immersion tests, the elastic modulus and yield strength of the porous iron remained in the range of the values reported for trabecular bone. Depending on the topological design of the specimens, AM porous iron appears to be widely cytocompatible. The observations reported here underline the importance of proper topological design in the development of AM porous biodegradable metals and suggest AM porous iron may be a highly attractive candidate for the development of future bone substitutes.

## Acknowledgements

The research for this paper was financially supported by the Prospero project, funded by the Interreg VA Flanders – The Netherlands program, CCI Grant No. 2014TC16RFCB04. Y.L. thanks the China Scholarship Council (CSC) for financial support. Richard Huizenga at the Department of Materials Science and Engineering of the Delft University of Technology is acknowledged for XRD analysis.

## Appendix A. Supplementary data

Supplementary data to this article can be found online at <https://doi.org/10.1016/j.actbio.2019.07.013>.

## References

- [1] A.A. Zadpoor, J. Malda, Additive manufacturing of biomaterials, tissues, and organs, *Ann. Biomed. Eng.* 45 (2017) 1–11.
- [2] L. Murr, S. Gaytan, F. Medina, H. Lopez, E. Martinez, B. Machado, D. Hernandez, L. Martinez, M. Lopez, R. Wicker, Next-generation biomedical implants using additive manufacturing of complex, cellular and functional mesh arrays, *Philos. Trans. R. Soc. London A: Math. Phys. Eng. Sci.* 368 (2010) 1999–2032.
- [3] A.A. Zadpoor, Mechanical performance of additively manufactured meta-biomaterials, *Acta Biomater.* 85 (2019) 41–59.
- [4] X. Wang, S. Xu, S. Zhou, W. Xu, M. Leary, P. Choong, M. Qian, M. Brandt, Y.M. Xie, Topological design and additive manufacturing of porous metals for bone scaffolds and orthopaedic implants: a review, *Biomaterials* 83 (2016) 127–141.
- [5] A.A. Zadpoor, Mechanics of additively manufactured biomaterials, *J. Mech. Behav. Biomed. Mater.* 70 (2017) 1–6.
- [6] A.H. Yusop, A.A. Bakir, N.A. Shaharom, M.R. Abdul Kadir, H. Hermawan, Porous biodegradable metals for hard tissue scaffolds: a review, *Int. J. Biomater.* 2012 (2012) 10.
- [7] S.M. Ahmadi, R. Hedayati, Y. Li, K. Lietaert, N. Tümer, A. Fatemi, C.D. Rans, B. Pouran, H. Weinans, A.A. Zadpoor, Fatigue performance of additively manufactured meta-biomaterials: the effects of topology and material type, *Acta Biomater.* 65 (2018) 292–304.
- [8] F. Bobbert, K. Lietaert, A. Eftekhari, B. Pouran, S. Ahmadi, H. Weinans, A. Zadpoor, Additively manufactured metallic porous biomaterials based on minimal surfaces: a unique combination of topological, mechanical, and mass transport properties, *Acta Biomater.* 53 (2017) 572–584.
- [9] S.M. Ahmadi, R. Kumar, E.V. Borisov, R. Petrov, S. Leeflang, Y. Li, N. Tümer, R. Huizenga, C. Ayas, A.A. Zadpoor, V.A. Popovich, From microstructural design to surface engineering: a tailored approach for improving fatigue life of additively manufactured meta-biomaterials, *Acta Biomater.* 83 (2019) 153–166.
- [10] C. Yan, L. Hao, A. Hussein, P. Young, D. Raymond, Advanced lightweight 316L stainless steel cellular lattice structures fabricated via selective laser melting, *Mater. Des.* 55 (2014) 533–541.
- [11] R. Hedayati, S.M. Ahmadi, K. Lietaert, B. Pouran, Y. Li, H. Weinans, C.D. Rans, A. A. Zadpoor, Isolated and modulated effects of topology and material type on the mechanical properties of additively manufactured porous biomaterials, *J. Mech. Behav. Biomed. Mater.* 79 (2018) 254–263.
- [12] R. Wauthle, J. van der Stok, S. Amin Yavari, J. Van Humbeeck, J.-P. Kruth, A.A. Zadpoor, H. Weinans, M. Mulier, J. Schrooten, Additively manufactured porous tantalum implants, *Acta Biomater.* 14 (2015) 217–225.
- [13] L.J. Gibson, Cellular solids, *MRS Bull.* 28 (2011) 270–274.
- [14] X. Miao, D. Sun, Graded/gradient porous biomaterials, *Materials* 3 (2009) 26–47.
- [15] A.A. Zadpoor, G. Campoli, H. Weinans, Neural network prediction of load from the morphology of trabecular bone, *Appl. Math. Model.* 37 (2013) 5260–5276.
- [16] J. Hazrati Marangalou, K. Ito, B. van Rietbergen, A novel approach to estimate trabecular bone anisotropy from stress tensors, *Biomech. Model Mechanobiol.* 14 (2015) 39–48.
- [17] D.M. Geraldes, A.T.M. Phillips, A comparative study of orthotropic and isotropic bone adaptation in the femur, *Int. J. Numer. Meth. Biomed. Eng.* 30 (2014) 873–889.
- [18] P. Christen, K. Ito, I. Knippels, R. Müller, G.H. van Lenthe, B. van Rietbergen, Subject-specific bone loading estimation in the human distal radius, *J. Biomech.* 46 (2013) 759–766.
- [19] G. Campoli, H. Weinans, A.A. Zadpoor, Computational load estimation of the femur, *J. Mech. Behav. Biomed. Mater.* 10 (2012) 108–119.
- [20] K. Nune, A. Kumar, R. Misra, S. Li, Y. Hao, R. Yang, Osteoblast functions in functionally graded Ti-6Al-4 V mesh structures, *J. Biomater. Appl.* 30 (2016) 1182–1204.
- [21] X.-Y. Zhang, G. Fang, S. Leeflang, A.A. Zadpoor, J. Zhou, Topological design, permeability and mechanical behavior of additively manufactured functionally graded porous metallic biomaterials, *Acta Biomater.* 84 (2019) 437–452.
- [22] K.C. Nune, A. Kumar, R.D.K. Misra, S.J. Li, Y.L. Hao, R. Yang, Functional response of osteoblasts in functionally gradient titanium alloy mesh arrays processed by 3D additive manufacturing, *Colloids Surf B Biointerfaces.* 150 (2017) 78–88.
- [23] J.M. Sobral, S.G. Caridade, R.A. Sousa, J.F. Mano, R.L. Reis, Three-dimensional plotted scaffolds with controlled pore size gradients: effect of scaffold geometry on mechanical performance and cell seeding efficiency, *Acta Biomater.* 7 (2011) 1009–1018.
- [24] S. Li, S. Zhao, W. Hou, C. Teng, Y. Hao, Y. Li, R. Yang, R.D.K. Misra, Functionally graded Ti-6Al-4V meshes with high strength and energy absorption, *Adv. Eng. Mater.* 18 (2016) 34–38.
- [25] S. Zhao, S.J. Li, S.G. Wang, W.T. Hou, Y. Li, L.C. Zhang, Y.L. Hao, R. Yang, R.D.K. Misra, L.E. Murr, Compressive and fatigue behavior of functionally graded Ti-6Al-4V meshes fabricated by electron beam melting, *Acta Mater.* 150 (2018) 1–15.
- [26] C. Han, Y. Li, Q. Wang, S. Wen, Q. Wei, C. Yan, L. Hao, J. Liu, Y. Shi, Continuous functionally graded porous titanium scaffolds manufactured by selective laser melting for bone implants, *J. Mech. Behav. Biomed. Mater.* 80 (2018) 119–127.
- [27] E. Onal, J. Frith, M. Jurg, X. Wu, A. Molotnikov, Mechanical properties and in vitro behavior of additively manufactured and functionally graded Ti6Al4V porous scaffolds, *Metals* 8 (2018) 200.
- [28] A. Di Luca, K. Szluzak, I. Lorenzo-Moldero, C.A. Ghebes, A. Lepedda, W. Swieszkowski, C. Van Blitterswijk, L. Moroni, Influencing chondrogenic differentiation of human mesenchymal stromal cells in scaffolds displaying a structural gradient in pore size, *Acta Biomater.* 36 (2016) 210–219.
- [29] E. Damien, K. Hing, S. Saeed, P.A. Revell, A preliminary study on the enhancement of the osteointegration of a novel synthetic hydroxyapatite scaffold in vivo, *J. Biomed. Mater. Res. A* 66A (2003) 241–246.
- [30] C. Erskens, D.M. Kalyon, H. Wang, Functionally graded electrospun polycaprolactone and  $\beta$ -tricalcium phosphate nanocomposites for tissue engineering applications, *Biomaterials* 29 (2008) 4065–4073.
- [31] M. Moravej, D. Mantovani, Biodegradable metals for cardiovascular stent application: interests and new opportunities, *Int. J. Mol. Sci.* 12 (2011) 4250.
- [32] R.O. Darouiche, Treatment of infections associated with surgical implants, *New Engl. J. Med.* 350 (2004) 1422–1429.
- [33] Y. Li, J. Zhou, P. Pavanram, M.A. Leeflang, L.I. Fockaert, B. Pouran, N. Tümer, K.U. Schröder, J.M.C. Mol, H. Weinans, H. Jahr, A.A. Zadpoor, Additively manufactured biodegradable porous magnesium, *Acta Biomater.* 67 (2018) 378–392.
- [34] Y. Li, H. Jahr, K. Lietaert, P. Pavanram, A. Yilmaz, L.I. Fockaert, M.A. Leeflang, B. Pouran, Y. Gonzalez-Garcia, H. Weinans, J.M.C. Mol, J. Zhou, A.A. Zadpoor, Additively manufactured biodegradable porous iron, *Acta Biomater.* 77 (2018) 380–393.
- [35] P. Wen, Y. Qin, Y. Chen, M. Voshage, L. Jauer, R. Poprawe, J. Henrich, Schleifenbaum, Laser additive manufacturing of Zn porous scaffolds: shielding gas flow, surface quality and densification, *J. Mater. Sci. Technol.* (2018).
- [36] D. Carluccio, A.G. Demir, L. Caprio, B. Previtali, M.J. Bermingham, M.S. Dargusch, The influence of laser processing parameters on the densification and surface morphology of pure Fe and Fe-35Mn scaffolds produced by selective laser melting, *J. Manuf. Process.* 40 (2019) 113–121.
- [37] Y. Li, H. Jahr, X.Y. Zhang, M.A. Leeflang, W. Li, B. Pouran, F.D. Tichelaar, H. Weinans, J. Zhou, A.A. Zadpoor, Biodegradation-affected fatigue behavior of additively manufactured porous magnesium, *Addit. Manuf.* 28 (2019) 299–311.
- [38] Y. Li, K. Lietaert, W. Li, X.Y. Zhang, M.A. Leeflang, J. Zhou, A.A. Zadpoor, Corrosion fatigue behavior of additively manufactured biodegradable porous iron, *Corros. Sci.* 156 (2019) 106–116.
- [39] J. He, F.-L. He, D.-W. Li, Y.-L. Liu, Y.-Y. Liu, Y.-J. Ye, D.-C. Yin, Advances in Fe-based biodegradable metallic materials, *RSC Adv.* 6 (2016) 112819–112838.
- [40] M. Peuster, C. Hesse, T. Schloo, C. Fink, P. Beerbaum, C. von Schnakenburg, Long-term biocompatibility of a corrodible peripheral iron stent in the porcine descending aorta, *Biomaterials* 27 (2006) 4955–4962.
- [41] T. Kraus, F. Moszner, S. Fischerauer, M. Fiedler, E. Martinelli, J. Eichler, F. Witte, E. Willbold, M. Schinhammer, M. Meischel, P.J. Uggowitzer, J.F. Löffler, A. Weinberg, Biodegradable Fe-based alloys for use in osteosynthesis: outcome of an in vivo study after 52 weeks, *Acta Biomater.* 10 (2014) 3346–3353.
- [42] I.A.J. van Hengel, M. Riool, L.E. Fratila-Apachitei, J. Witte-Bouma, E. Farrell, A.A. Zadpoor, S.A.J. Zaai, I. Apachitei, Selective laser melting porous metallic implants with immobilized silver nanoparticles kill and prevent biofilm formation by methicillin-resistant *Staphylococcus aureus*, *Biomaterials* 140 (2017) 1–15.

- [43] F. Pennella, G. Cerino, D. Massai, D. Gallo, G. Falvo D'Urso Labate, A. Schiavi, M. A. Deriu, A. Audenino, U. Morbiducci, A survey of methods for the evaluation of tissue engineering scaffold permeability, *Ann. Biomed. Eng.* 41 (2013) 2027–2041.
- [44] A. Oyane, H.-M. Kim, T. Furuya, T. Kokubo, T. Miyazaki, T. Nakamura, Preparation and assessment of revised simulated body fluids, *J. Biomed. Mater. Res. A* 65A (2003) 188–195.
- [45] F. Zhao, B. van Rietbergen, K. Ito, S. Hofmann, Flow rates in perfusion bioreactors to maximise mineralisation in bone tissue engineering in vitro, *J. Biomech.* 79 (2018) 232–237.
- [46] M.E. Gomes, V.I. Sikavitsas, E. Behraves, R.L. Reis, A.G. Mikos, Effect of flow perfusion on the osteogenic differentiation of bone marrow stromal cells cultured on starch-based three-dimensional scaffolds, *J. Biomed. Mater. Res. A* 67A (2003) 87–95.
- [47] J.R. Vetsch, D.C. Betts, R. Müller, S. Hofmann, Flow velocity-driven differentiation of human mesenchymal stromal cells in silk fibroin scaffolds: a combined experimental and computational approach, *PLoS One* 12 (2017).
- [48] T. Huang, J. Cheng, Y.F. Zheng, In vitro degradation and biocompatibility of Fe-Pd and Fe-Pt composites fabricated by spark plasma sintering, *Mater. Sci. Eng. C* 35 (2014) 43–53.
- [49] B. Song, X. Zhao, S. Li, C. Han, Q. Wei, S. Wen, J. Liu, Y. Shi, Differences in microstructure and properties between selective laser melting and traditional manufacturing for fabrication of metal parts: a review, *Front. Mech. Eng.* 10 (2015) 111–125.
- [50] L.-E. Loh, C.-K. Chua, W.-Y. Yeong, J. Song, M. Mapar, S.-L. Sing, Z.-H. Liu, D.-Q. Zhang, Numerical investigation and an effective modelling on the Selective Laser Melting (SLM) process with aluminium alloy 6061, *Int. J. Heat Mass Transf.* 80 (2015) 288–300.
- [51] A. Simchi, H. Pohl, Effects of laser sintering processing parameters on the microstructure and densification of iron powder, *Mater. Sci. Eng. A* 359 (2003) 119–128.
- [52] B. Song, S. Dong, Q. Liu, H. Liao, C. Coddet, Vacuum heat treatment of iron parts produced by selective laser melting: microstructure, residual stress and tensile behavior, *Mater. Des.* 54 (2014) 727–733.
- [53] S. Truscello, G. Kerckhofs, S. Van Bael, G. Pyka, J. Schrooten, H. Van Oosterwyck, Prediction of permeability of regular scaffolds for skeletal tissue engineering: a combined computational and experimental study, *Acta Biomater.* 8 (2012) 1648–1658.
- [54] H. Montazerian, M. Zhanmanesh, E. Davoodi, A.S. Milani, M. Hoorfar, Longitudinal and radial permeability analysis of additively manufactured porous scaffolds: effect of pore shape and porosity, *Mater. Des.* 122 (2017) 146–156.
- [55] D. Ali, S. Sen, Finite element analysis of mechanical behavior, permeability and fluid induced wall shear stress of high porosity scaffolds with gyroid and lattice-based architectures, *J. Mech. Behav. Biomed. Mater.* 75 (2017) 262–270.
- [56] F.P.W. Melchels, B. Tonnarelli, A.L. Olivares, I. Martin, D. Lacroix, J. Feijen, D.J. Wendt, D.W. Grijpma, The influence of the scaffold design on the distribution of adhering cells after perfusion cell seeding, *Biomaterials* 32 (2011) 2878–2884.
- [57] B. Liu, Y.F. Zheng, Effects of alloying elements (Mn, Co, Al, W, Sn, B, C and S) on biodegradability and in vitro biocompatibility of pure iron, *Acta Biomater.* 7 (2011) 1407–1420.
- [58] J.C. Atherton, Acid–base balance: maintenance of plasma pH, *Anaesthesia Intensive Care Med.* 10 (2009) 557–561.
- [59] A.P.Md Saad, N. Jasmawati, M.N. Harun, M.R. Abdul Kadir, H. Nur, H. Hermawan, A. Syahrom, Dynamic degradation of porous magnesium under a simulated environment of human cancellous bone, *Corros. Sci.* 112 (2016) 495–506.
- [60] C.S. Obayi, R. Tolouei, C. Paternoster, S. Turgeon, B.A. Okorie, D.O. Obikwelu, G. Cassar, J. Buhagiar, D. Mantovani, Influence of cross-rolling on the microstructure and biodegradation of pure iron as biodegradable material for medical implants, *Acta Biomater.* 17 (2015) 68–77.
- [61] M. Moravej, F. Prima, M. Fiset, D. Mantovani, Electroformed iron as new biomaterial for degradable stents: development process and structure–properties relationship, *Acta Biomater.* 6 (2010) 1726–1735.
- [62] M. Moravej, A. Purnama, M. Fiset, J. Couet, D. Mantovani, Electroformed pure iron as a new biomaterial for degradable stents: in vitro degradation and preliminary cell viability studies, *Acta Biomater.* 6 (2010) 1843–1851.
- [63] F. Witte, N. Hort, C. Vogt, S. Cohen, K.U. Kainer, R. Willumeit, F. Feyerabend, Degradable biomaterials based on magnesium corrosion, *Curr. Opin. Solid State Mater. Sci.* 12 (2008) 63–72.
- [64] C.S. Obayi, R. Tolouei, A. Mostavan, C. Paternoster, S. Turgeon, B.A. Okorie, D.O. Obikwelu, D. Mantovani, Effect of grain sizes on mechanical properties and biodegradation behavior of pure iron for cardiovascular stent application, *Biomater* 6 (2016).
- [65] M. Moravej, S. Amira, F. Prima, A. Rahem, M. Fiset, D. Mantovani, Effect of electrodeposition current density on the microstructure and the degradation of electroformed iron for degradable stents, *Mater. Sci. Eng. B* 176 (2011) 1812–1822.
- [66] E. Zhang, H. Chen, F. Shen, Biocorrosion properties and blood and cell compatibility of pure iron as a biodegradable biomaterial, *J. Mater. Sci. – Mater. Med.* 21 (2010) 2151–2163.
- [67] J. Capek, Š. Msallamová, E. Jablonská, J. Lipov, D. Vojtěch, A novel high-strength and highly corrosive biodegradable Fe-Pd alloy: structural, mechanical and in vitro corrosion and cytotoxicity study, *Mater. Sci. Eng. C* 79 (2017) 550–562.
- [68] W. Lin, L. Qin, H. Qi, D. Zhang, G. Zhang, R. Gao, H. Qiu, Y. Xia, P. Cao, X. Wang, W. Zheng, Long-term in vivo corrosion behavior, biocompatibility and bioresorption mechanism of a bioresorbable nitrided iron scaffold, *Acta Biomater.* 54 (2017) 454–468.
- [69] P. Mariot, M.A. Leeflang, L. Schaeffer, J. Zhou, An investigation on the properties of injection-molded pure iron potentially for biodegradable stent application, *Powder Technol.* 294 (2016) 226–235.
- [70] J. Parthasarathy, B. Starly, S. Raman, A. Christensen, Mechanical evaluation of porous titanium (Ti6Al4V) structures with electron beam melting (EBM), *J. Mech. Behav. Biomed. Mater.* 3 (2010) 249–259.
- [71] M. Yazdimamaghani, M. Razavi, D. Vashae, K. Moharamzadeh, A.R. Boccaccini, L. Tayebi, Porous magnesium-based scaffolds for tissue engineering, *Mater. Sci. Eng. C* 71 (2017) 1253–1266.
- [72] S. Ahmadi, S. Yavari, R. Wauthle, B. Pouran, J. Schrooten, H. Weinans, A. Zadpoor, Additively manufactured open-cell porous biomaterials made from six different space-filling unit cells: the mechanical and morphological properties, *Materials* 8 (2015) 1871.
- [73] R. Wauthle, S.M. Ahmadi, S. Amin Yavari, M. Mulier, A.A. Zadpoor, H. Weinans, J. Van Humbeeck, J.-P. Kruth, J. Schrooten, Revival of pure titanium for dynamically loaded porous implants using additive manufacturing, *Mater. Sci. Eng. C* 54 (2015) 94–100.
- [74] S.J. Hollister, Scaffold design and manufacturing: from concept to clinic, *Adv. Mater.* 21 (2009) 3330–3342.
- [75] S.J. Hollister, Porous scaffold design for tissue engineering, *Nat. Mater.* 4 (2005) 518–524.
- [76] J. Fischer, D. Pröfrock, N. Hort, R. Willumeit, F. Feyerabend, Reprint of: improved cytotoxicity testing of magnesium materials, *Mater. Sci. Eng. B* 176 (2011) 1773–1777.
- [77] J. Wang, F. Witte, T. Xi, Y. Zheng, K. Yang, Y. Yang, D. Zhao, J. Meng, Y. Li, W. Li, K. Chan, L. Qin, Recommendation for modifying current cytotoxicity testing standards for biodegradable magnesium-based materials, *Acta Biomater.* 21 (2015) 237–249.
- [78] X. Liu, D.P. Rodeheaver, J.C. White, A.M. Wright, L.M. Walker, F. Zhang, S. Shannon, A comparison of in vitro cytotoxicity assays in medical device regulatory studies, *Regul. Toxicol. Pharm.* 97 (2018) 24–32.
- [79] H. Meng, X. Zhang, Q. Chen, J. Wei, Y. Wang, A. Dong, H. Yang, T. Tan, H. Cao, Preparation of poly (aspartic acid) superabsorbent hydrogels by solvent-free processes, *J. Polym. Eng.* 35 (2015) 647–655.
- [80] S. Zhu, N. Huang, L. Xu, Y. Zhang, H. Liu, H. Sun, Y. Leng, Biocompatibility of pure iron: in vitro assessment of degradation kinetics and cytotoxicity on endothelial cells, *Mater. Sci. Eng. C* 29 (2009) 1589–1592.
- [81] R.S. Britton, K.L. Leicester, B.R. Bacon, Iron Toxicity and Chelation Therapy, *Int. J. Hematol.* 76 (2002) 219–228.
- [82] A. Francis, Y. Yang, S. Virtanen, A.R. Boccaccini, Iron and iron-based alloys for temporary cardiovascular applications, *J. Mater. Sci. – Mater. Med.* 26 (2015) 138.
- [83] M. Peuster, P. Wohlsein, M. Brüggmann, M. Ehlerding, K. Seidler, C. Fink, H. Brauer, A. Fischer, G. Hausdorf, A novel approach to temporary stenting: degradable cardiovascular stents produced from corrodible metal—results 6–18 months after implantation into New Zealand white rabbits, *Heart* 86 (2001) 563–569.
- [84] D. Andreas, H. Thomas, B.F. Wilhelm, P. Matthias, In vitro and in vivo corrosion properties of new iron–manganese alloys designed for cardiovascular applications, *J. Biomed. Mater. Res. B Appl. Biomater.* 103 (2015) 649–660.
- [85] A. Di Luca, B. Ostrowska, I. Lorenzo-Molero, A. Lepedda, W. Swieszkowski, C. Van Blitterswijk, L. Moroni, Gradients in pore size enhance the osteogenic differentiation of human mesenchymal stromal cells in three-dimensional scaffolds, *Sci. Rep.* 6 (2016) 22898.